Petroleum Science 23 (2026) 5738–5756

Contents lists available at ScienceDirect

Petroleum Science

journal homepage: www.keaipublishing.com/en/journals/petroleum-science

Original Paper

Effects of initial damage degrees on crack propagation and permeability characteristics of coal subjected to cyclic loading

Qi-Can Ran [a,b,c], Yun-Pei Liang [a,b,*], Chun-Feng Ye [a,b,**], Teng-Fei Ma [a,b], Zi-Han Chen [d]

[a] State Key Laboratory of Coal Mine Disaster Dynamics and Control, Chongqing University, Chongqing, 400044, China
[b] School of Resources and Safety Engineering, Chongqing University, Chongqing, 400044, China
[c] School of Mines, China University of Mining and Technology, Xuzhou, 221116, Jiangsu, China
[d] NBK Institute of Mining Engineering, The University of British Columbia, Vancouver, BC, V6T 1Z4, Canada

ARTICLE INFO

Article history:
Received 18 August 2025
Received in revised form
26 January 2026
Accepted 5 June 2026
Available online 11 June 2026

Edited by Xiu-Fang Hu

Keywords:
Acoustic emission
Dissipated energy
Crack propagation
Fractal dimension
Computed tomography

ABSTRACT

Once deep coal rock is disturbed by engineering operations, coal exhibits different initial damage degrees (IDDs), which may govern subsequent crack propagation and permeability evolution under cyclic stress. Therefore, cyclic loading and permeability tests, combined with acoustic emission (AE) and computed tomography (CT) scanning techniques, were conducted to systematically investigate the effects of the IDD on the crack propagation and permeability evolution of coal. The results indicated that high IDDs led to a significant decrease in the peak strength and deformation modulus of the coal samples and a significant increase in the dissipated energy percentage. Furthermore, AE analyses showed that the *b* value dropped from 1.863 to 0.784 and the energy critical index decreased, whereas the multifractal spectrum width and subset parameter increased, indicating a shift from small-scale microcracking to more complex, large-scale crack coalescence in coal specimens with higher IDDs. Permeability generally decreased with increasing stress, but coal specimens with high IDDs exhibited a transient permeability recovery at high stress levels and a larger post-failure permeability enhancement, reflecting the competition between compaction and crack propagation. Moreover, CT-based analysis shows that crack volume percentage increased from 2.821% to 8.968% and fractal dimension rose from 2.011 to 2.052 with increasing IDDs, correlating well with permeability evolution. These results provide useful implications for stability and permeability characteristics in coal reservoirs and deep geo-energy engineering.

1. Introduction

Coal seams are not only sources of solid energy (He et al., 2025c; Wu et al., 2025a; Zhao et al., 2026), but also important unconventional reservoirs for coalbed methane (CBM) and underground gas storage (Cui et al., 2025; Fan et al., 2025; Zou et al., 2025a). Their permeability behavior and crack connectivity directly control gas producibility, injectivity and long-term storage security (Chen et al., 2025; Wang et al., 2026; Zhang et al., 2025c). During CBM production operations, coal seams often experience cyclic stress paths rather than monotonic loading. Therefore, understanding how coal cracks propagate and how permeability evolves under cyclic loading is directly relevant to petroleum engineering problems. Another critical but often overlooked aspect is that coal near the wellbore rarely remains intact. Initial damage (pre-existing microcracks and defects) can be generated by drilling or stress redistribution around openings (Dai et al., 2024; Guo et al., 2025a), where coal may exhibit different initial damage degrees (IDDs) (He et al., 2025d; Huang et al., 2021a). IDDs can strongly influence subsequent cyclic deformation and failure, thereby reshaping fracture connectivity and permeability evolution. Consequently, a fundamental understanding of how IDDs affect crack network evolution and permeability in coal under cyclic loading is also of direct relevance to the geomechanical

* Corresponding author.
** Corresponding author.
E-mail addresses: liangyunpei@126.com (Y.-P. Liang), chunfeng.ye@cqu.edu.cn (C.-F. Ye).
Peer review under the responsibility of China University of Petroleum (Beijing).

https://doi.org/10.1016/j.petsci.2026.06.011
1995-8226/

design and risk assessment of deep petroleum and geoenergy engineering projects.

Consequently, many scholars have conducted in-depth studies on the mechanical behaviors of coal and rock materials under loading (Guo et al., 2025b; He et al., 2025e; Li et al., 2025; Zhang et al., 2025b). For example, Xu et al. (2025) revealed that kyanite conformed to specific energy storage and dissipation patterns at different lamination angles. Yang et al. (2024) found that cracks play a key role in affecting the brittleness, strength, and failure patterns of rocks by introducing different numbers of cracks. In addition, pioneering studies have been conducted on materials with initial damage (Hou et al., 2019; Yu et al., 2022). Zhang et al. (2023) showed that as the number of cycles increased, the bearing capacity and elastic modulus were significantly reduced if the sandstone had suffered greater initial damage. Lei et al. (2023) found that the compressive and tensile strengths of initially damaged materials were significantly reduced. Miao et al. (2024) found that an increase in the initial damage led to a decrease in the uniaxial compressive strength and simultaneously triggered a gradual increase in the horizontal strain. However, although the aforementioned studies provide a good foundation for the mechanical characterization of initially damaged materials (Jiang et al., 2020) the effects of initial damage on crack propagation within coal and the evolution of the crack network throughout the loading history in a triaxial cyclic loading environment still require further exploration. Notably, the acoustic emission (AE) method enables real-time tracking of crack initiation and development (Wu et al., 2025b; Ye et al., 2026a; Zhang et al., 2026a; Zhu et al., 2025), and computed tomography (CT) scanning can visually characterize the spatial distribution of cracks inside samples (Liu et al., 2024b; Zhang et al., 2024a). Thus, the combination of the two offers outstanding research value for revealing crack propagation mechanisms.

Permeability evolution serves as a key measure of the efficiency of gas transport in coal seams and has thus received extensive attention from researchers (He et al., 2025a; Yang et al., 2025; Zhang et al., 2026b). Guo et al. (2019) obtained the variation rule of coal seam permeability under plastic flow conditions by performing permeability tests on coal samples after shear yielding under cyclic loading conditions. Meanwhile, Liu et al. (2024a) found that coal under high stress conditions at low reservoir pressure states was mainly affected by slip effects via gas-containing raw coal seepage tests. Zhang et al. (2017) conducted triaxial seepage tests on gas-containing coal by unloading the confining pressure to simulate the excavation of coal seams, and they elucidated a three-stage characterization of the gas seepage properties of raw coal. Wang et al. (2024) established a permeability evolution pattern based on the damage variable of the axial strain and effectively characterized the permeability evolution pattern using the damage variable. Jiang et al. (2017) investigated how permeability of raw coal evolves during graded cyclic loading conditions. Fan and Liu (2019) conducted cyclic loading experiments on raw coal specimens and introduced the concept of average permeability damage to quantify the effects of the maximum stress, loading path, and gas type on permeability damage. Niu et al. (2024) performed true triaxial seepage testing on columnar jointed basalt, revealing a correlation involving the permeability. And they found that the relationship between the permeability and axial stress of specimens conformed to a power exponential relationship and that the evolution of permeability was closely correlated with the degree of damage. Zou et al. (2016) examined the permeability characteristics of parallel-stratified and vertical-stratified coal samples under cyclic loading. In summary, these studies provide important references for understanding the permeability behavior of coal under single or cyclic loading and unloading conditions. However, systematic studies on the changes in permeability characteristics, considering the differences in the IDDs of coal samples, are still scarce.

In summary, these studies made valuable contributions; however, some critical gaps remain. Although many studies have been conducted on the mechanical behavior and permeability evolution of coal and rock under cyclic loading, few studies have directly compared the effects of different IDDs on crack propagation and permeability evolution in coal. Moreover, dynamic monitoring technology combined with traditional mechanical testing for the full elucidation of the potential failure mechanisms of coal samples with different IDDs is lacking. The IDD not only affects the development and propagation of the crack network within coal but also has a profound effect on the fluid transport channel and thereby causes the permeability to show a differentiated evolution pattern at different stages of cyclic loading. However, there is still insufficient research on how IDD affects the crack propagation and permeability change mechanism of coal under cyclic loading. Therefore, this study aims to remedy these deficiencies by employing an integrated experimental approach that combines mechanical testing, permeability testing, AE monitoring, and CT scanning to gain a deeper understanding of the interactions between the initial damage, crack network evolution, and permeability changes in coal samples.

Accordingly, cyclic loading experiments and permeability tests on coal samples with different IDDs were performed and then this study combined them with AE monitoring and CT scanning for comprehensive analysis. First, the mechanical properties of coal with different IDDs were obtained. Subsequently, the crack propagation characteristics and permeability changes in the coal samples were determined. Finally, the crack distribution characteristics, permeability dynamic changes, and their mechanisms were systematically investigated by combining the mechanical response, AE monitoring, and CT scanning. This study makes several novel contributions. First, by combining conventional mechanical indicators with a suite of AE statistics, the IDD-dependent transition from dispersed microcracking to large-scale crack coalescence is dynamically characterized. Second, the permeability evolution under cyclic loading is clarified, revealing the competition between compaction and crack propagation. Third, post-failure CT scanning is used to quantify crack, and regression analyses establish quantitative links between these CT-derived fracture attributes and the permeability enhancement. The research results provide new experimental evidence and theoretical references for understanding the deformation failure and seepage behavior of coal seams under complex stress conditions, and offer a scientific basis for improving the geomechanical evaluation of CBM recovery and other deep geoenergy and petroleum engineering applications involving cyclic loading.

2. Methods

2.1. Coal samples and experimental systems

The coal samples used in this test were selected from the same coal rock stratum and collected from a coal mine located in the Xinjiang Uygur Autonomous Region, China, with a uniform and dense texture and no evident joints or fractures. After fine grinding, the samples were uniform and fine in appearance. The two end surfaces were smooth and even. Furthermore, samples were prepared as cylinders with an aspect ratio of approximately 2:1. Specifically, the diameter of the specimens used in this test was approximately 50 mm, and the height was approximately 100 mm, thus ensuring that the standard size requirements were met. Moreover, the coal samples were mainly composed of kaolinite, quartz, chlorite, and nisbite, as determined by X-ray diffraction (XRD), as shown in Fig. 1(a). Before the formal test, the prepared specimens were strictly screened to minimize the influence of coal dispersion on the test results. First, an ultrasonic equipment was used to measure the P-wave velocity in each coal sample. Second, the selected samples were weighed accurately using an analytical balance with an accuracy of ±0.01 g. This high-precision weighing ensured that the sample quality could be compared and controlled effectively. Via the aforementioned screening and control measures, the reliability and comparability of subsequent test data can be effectively improved. Table 1 presents the fundamental characteristics of coal samples. Triaxial compression experiments were conducted using the experimental equipment below at a loading rate of 0.2 mm/min. According to the results of mechanical property tests that were completed in advance, the coal samples exhibited a triaxial compressive strength (TCS) of 55.50 MPa under a confining pressure of 5 MPa.

The experimental setup used in this study is shown in Fig. 1. This test adopted a variety of high-precision experimental equipment and testing methods to comprehensively obtain the mechanical properties and seepage patterns of the coal samples. As shown in Fig. 1(b), the main loading equipment was an RTX-3000 rock mechanics test system (GCTS, USA). The test system had independent axial and radial mechanical control modules that controlled the axial and radial stress states of the specimen by stress or displacement, respectively. The displacement control mode was used in this experiment. Meanwhile, the system was equipped with an independent permeability gas injection module that could inject gas into the sample and perform permeability testing. In addition, a PCI-2 acoustic emission (AE) system was used to monitor the coal samples in real time during the loading process, as shown in Fig. 1(b). In this study, four AE sensors were arranged circumferentially at approximately 90° intervals on the loading platens to maximize signal capture and reduce azimuthal bias. Prior to installation, the contact surfaces were polished and cleaned with ethanol. A thin layer of Vaseline coupling agent was applied between each sensor and the platen to ensure stable acoustic coupling. The sensors were then fixed using elastic bands to maintain constant contact pressure throughout the test. Coupling quality was checked before each test, and sensors were re-coupled if abnormal attenuation or missing hits were observed. In the experiments, the sampling frequency of the AE signals was set to 1.0 MHz. Noise reduction was carried out through both hardware settings and data post-processing. A pre-amplification of 40 dB and a band-pass filter of 20–400 kHz were adopted in the PCI-2 system to suppress low-frequency mechanical noise and high-frequency electrical noise. During an initial period before loading, the trigger threshold was set to 40 dB, which is significantly higher than the maximum background noise level. In addition, to further understand the specific morphology and distribution characteristics of crack propagation inside the coal samples on a spatial scale, CT scanning was performed on the coal samples after failure at the end of the loading test, as shown in Fig. 1(c). SOMATOM Scope CT scanning system was manufactured by Siemens Shanghai Medical Equipment Co., Ltd. The CT scanning device offers a spatial resolution of 0.35 mm. A comparison and analysis of the CT scanning results with the previous AE data not only verified the crack propagation process monitored by AE but also provided quantitative support for the subsequent study of the coal failure mechanism.

Table 1
Basic parameters and loading program of coal samples.

Group	No.	Diameter, mm	Height, mm	Mass, g	P-wave velocity, m/s	Initial damage loading paths
Group-1	CS-1	49.85	99.85	253.32	2040	-
	CS-2	49.86	99.93	252.87	2040	IDLP-1
	CS-3	49.86	99.81	251.53	2040	IDLP-2
	CS-4	49.85	99.91	254.51	2130	IDLP-3
Group-2	CS-5	49.80	99.98	254.76	2150	-
	CS-6	49.84	99.92	253.77	2130	IDLP-1
	CS-7	49.87	99.83	252.43	2050	IDLP-2
	CS-8	49.86	99.93	252.87	2040	IDLP-3

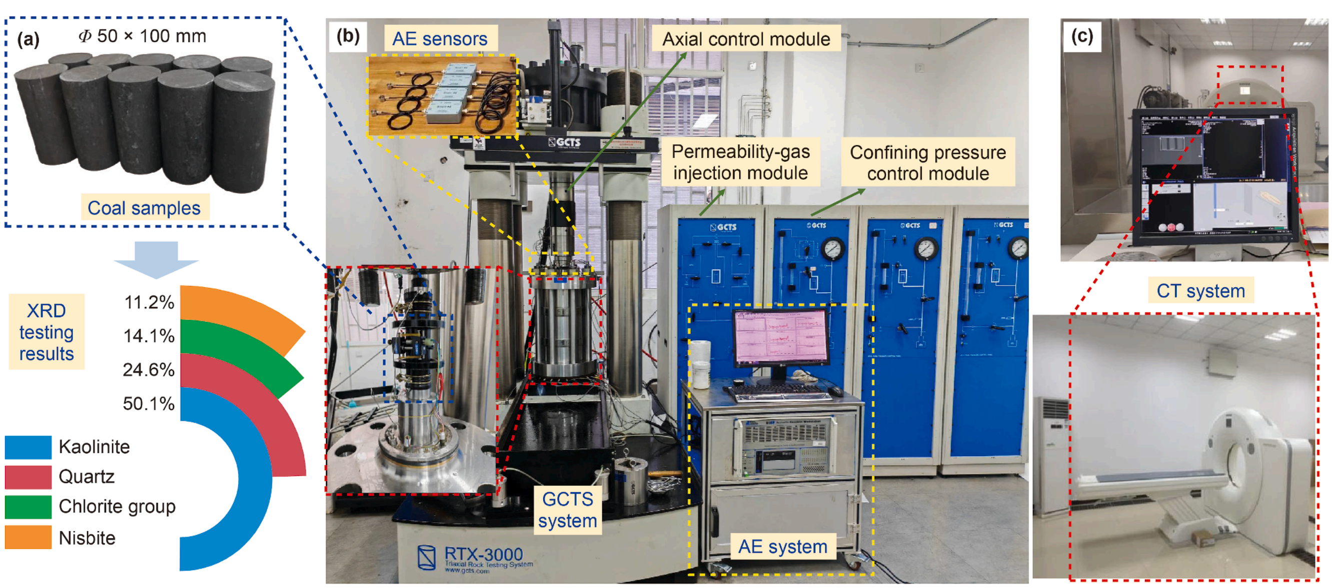

Fig. 1. Experimental samples and systems. **(a)** Coal samples; **(b)** rock mechanics and permeability testing system with AE system; **(c)** CT scanning system.

2.2. Preparation of coal samples with different IDDs

2.2.1. Loading paths of preparing different IDDs

A preloading method involving cyclic loading was used to obtain coal samples with different IDDs. In previous studies, scholars have often introduced initial damage to coal samples via cyclic loading. The cyclic loading paths cause initial damage to the coal samples, and the greater the number of cycles, the greater the degree of accumulation of the initial damage (Zhang et al., 2024b). Consequently, three different initial damage loading paths were established in this experiment to treat the coal samples by sequentially increasing the upper limit stress level while maintaining a constant lower limit stress.

During the initial damage preparation stage, all preloading tests were conducted on the same triaxial loading system as described in Section 2.1. A constant confining pressure of 5 MPa was first applied and maintained throughout the whole preloading process. The deviatoric stress was then applied under displacement control. The axial loading rate was set to 0.2 mm/min and the unloading rate was 0.4 mm/min, which are identical to those used in the subsequent cyclic loading and permeability tests. During the experiment, the lower limit of the deviatoric stress was fixed at 5% TCS (2.775 MPa), whereas the upper limit of the deviatoric stress was increased step-by-step with an amplitude of 10% TCS (5.550 MPa) in each cycle. The specific settings were as follows. IDLP-1 path: 4 cycles of loading and unloading, and the final upper stress reached 45% TCS (24.995 MPa); IDLP-2 path: 6 cycles, and the final upper stress reached 65% TCS (36.075 MPa); and IDLP-3 path: 7 cycles, and the final upper stress reached 75% TCS (41.625 MPa). Within each cycle of the IDLP-1 to IDLP-3 paths, the deviatoric stress was increased from the prescribed lower limit to the upper limit and then unloaded back to the lower limit without an additional holding stage. The selection of the stress upper limits was mainly based on the following considerations (Taheri et al., 2020): according to the damage evolution law of coal and rock, an upper limit of 45% TCS can induce the initiation of microcracks without significant propagation, thus introducing only slight initial damage. When the stress upper limit reaches 65% TCS, some cracks begin to propagate stably, forming a moderately damaged structure. Whereas at 75% TCS, the coal approaches the crack damage threshold, and the internal fracture network is highly developed, representing a severely damaged state. Therefore, by controlling the number of cycles and the stress upper limits under different loading paths, different levels of initial damage were effectively introduced into the coal specimens.

The specimens prepared using the above method had already developed internal microcracks to varying degrees, forming an initially damaged structure. Previous studies have reported the occurrence of distinct surface macrocracks during the preparation of coal with initial damage (Yin et al., 2023), which confirms that microcracks are generated in the coal as a result of the initial damage treatment. Using the aforementioned initial damage-loading paths, three coal samples with different IDDs were obtained separately. Subsequently, the preloaded coal samples were compared to the original coal samples without preloading. This approach can effectively evaluate the effects of different IDDs on the subsequent mechanical patterns of coal samples.

2.2.2. Definition of initial damage variable

During cyclic loading, the coal sample damage evolution process is inevitably accompanied by interconversion between the input energy, elastic energy, and dissipated energy (Kong et al., 2022; Li et al., 2023; Zou et al., 2025b). Therefore, the research defines the initial damage variables for coal subjected to cyclic loading conditions, considering energy dissipation.

Fig. 2 shows the schematic stress–strain curves of the coal after a single loading and unloading (Zhao et al., 2026). Among them, section *AB* is the loading curve $f_1(\varepsilon)$, and section *BC* is the unloading curve $f_2(\varepsilon)$. As shown in Fig. 2, according to the first thermodynamic pattern, the total input energy (U_t) produced by the internal and external forces per unit volume of coal specimens during a single loading and unloading test is represented by the area bounded by the loading curve *AB* and the *x*-axis, that is, S_{DABFD}. The elastic energy (U_e) released during the unloading phase corresponds to the region enclosed by the unloading curve *BC* and the *x*-axis, that is, S_{ECBFE}. Therefore, the dissipated energy (U_d) consumed by the damaged coal during a single loading and unloading is the difference between the U_t and U_e, that is, the green-shaded area S_{DABCED} in Fig. 2. The U_t, U_e, and U_d terms were calculated using Eq. (1):

$$\begin{cases} U_t = \int_{\varepsilon'}^{\varepsilon''} f_1(\varepsilon)\mathrm{d}\varepsilon \\ U_e = \int_{\varepsilon'''}^{\varepsilon''} f_2(\varepsilon)\mathrm{d}\varepsilon \\ U_d = U_t - U_e = \int_{\varepsilon'}^{\varepsilon''} f_1(\varepsilon)\mathrm{d}\varepsilon - \int_{\varepsilon'''}^{\varepsilon''} f_2(\varepsilon)\mathrm{d}\varepsilon \end{cases}, \tag{1}$$

where ε', ε'', and ε''' denote the strains corresponding to points *D*, *F*, and *E*, respectively.

The number of macroscopic cracks on the coal sample surface increased after the initial damage treatment (Yin et al., 2023). However, intuitive features cannot quantitatively characterize the IDDs of coal samples. The damage variables characterize the internal condition of coal and enable quantitative evaluation of crack evolution. The initial damage variable (D_{ini}) is defined according to the energy method, as shown in Eq. (2) (Huang et al., 2021b). The range of D_{ini} ranges from 0 to 1. Without changing the lower limit of the cyclic stress in the cyclic loading and unloading test, the calculation method of D_{ini} defined in Eq. (2) considers the influences of cyclic numbers, which can better reflect the actual damage conditions of the samples:

$$D_{ini} = \sum_{k=1}^{i} {U_d}^k \Big/ \left(\sum_{k=1}^{i} {U_d}^k + {U_e}^k \right), \tag{2}$$

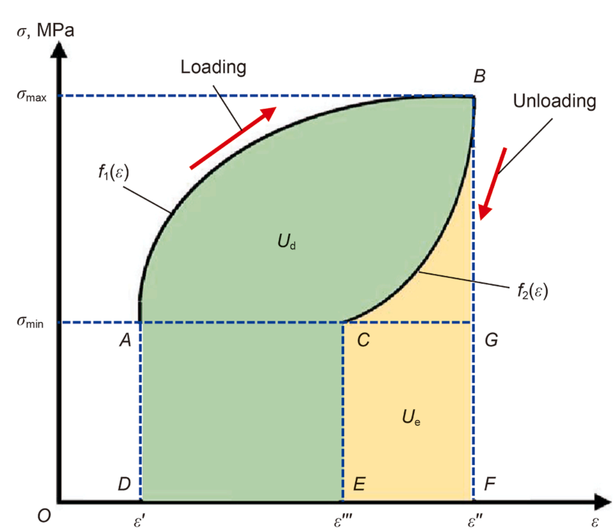

Fig. 2. Method of strain energy calculation under a single loading and unloading cycle (Liang et al., 2022).

where D_{ini} is the initial damage variable; U_d^k is the energy dissipated in the k^{th} cycle, MJ/m^3; and U_e^k is the elastic energy generated in the k^{th} cycle, MJ/m^3.

To clearly capture the strain energy characteristics and the evolution of D_{ini}, only the axial deformation was considered in the calculation of the strain energy. Moreover, taking CS-2, CS-3, and CS-4 samples of Group-1 in Table 1 as examples, the corresponding strain–energy characteristics are shown in Fig. 3. Furthermore, the variation patterns of D_{ini} with the number of cycles in each cyclic loading range were obtained using Eq. (2) (Fig. 3). With increasing cyclic number, the D_{ini} coefficients of the coal samples with varying loading stress levels gradually increased. The values of D_{ini} varied between 0 and 1, which is in line with the definition of D_{ini}.

2.3. Loading programs and permeability tests

In this research, the mechanical response of coal and evolution of its permeability properties under different IDDs were investigated using multilevel cyclic loading experiments. The experimental program is shown in Fig. 4(a) and includes two main parts: the cyclic loading path and the permeability test. First, a 5 MPa confining pressure was applied to the coal samples and maintained constant. Subsequently, the deviatoric stress was loaded to 16.65 MPa (the lower limit of level 1), and cyclic loading and unloading were started with an amplitude of 11.10 MPa. That is, the upper limit of the cycle was 27.75 MPa, and the number of cycles was five. At level 2, cyclic loading and unloading began with a magnitude of 11.10 MPa, a lower limit of 27.75 MPa, an upper limit of 38.85 MPa, and 5 cycles. By analogy, cyclic loading continued until the failure of the samples. The loading rate was set to 0.2 mm/min, and the unloading rate was 0.4 mm/min during the entire test.

The permeability of the coal samples was tested at the end of each cycle of loading and unloading as well as after the failures of the samples, shown as green dots in Fig. 4(a). To avoid the influence of the test medium pressure on the stress field of the samples during the test, the transient pressure pulse method was used for the permeability test. The test medium was low-pressure carbon dioxide. Using the differential pressure sensor in the permeability test module in the experimental system, the pressure difference between the two ends of each sample was recorded in real time, and the sample permeability was calculated using Eq. (3) (Liu et al., 2023):

$$k = -\frac{V\mu L \ln\left(\frac{P_{\Delta t}}{P_{\Delta t_0}}\right)}{\overline{Z}A(P_{0u}+P_{0d})\Delta t}, \tag{3}$$

where k is the permeability, m^2; μ is the viscosity coefficient of low-pressure carbon dioxide, set to 1.5×10^{-5} Pa·s; $\overline{Z}$ is the average compression factor, set to 1; V is the volume of the gas tank of the specimen, m^3 (the volume of the gas tank used in the test is 0.0025 m^3); $P_{\Delta t_0}$ and $P_{\Delta t}$ are the pressure differences between the initial and t moments of samples, Pa; A is the cross-section of the samples, m^2; L is the length of samples, m; Δt is the time interval of the test, which indicates the time from the initial state to a certain

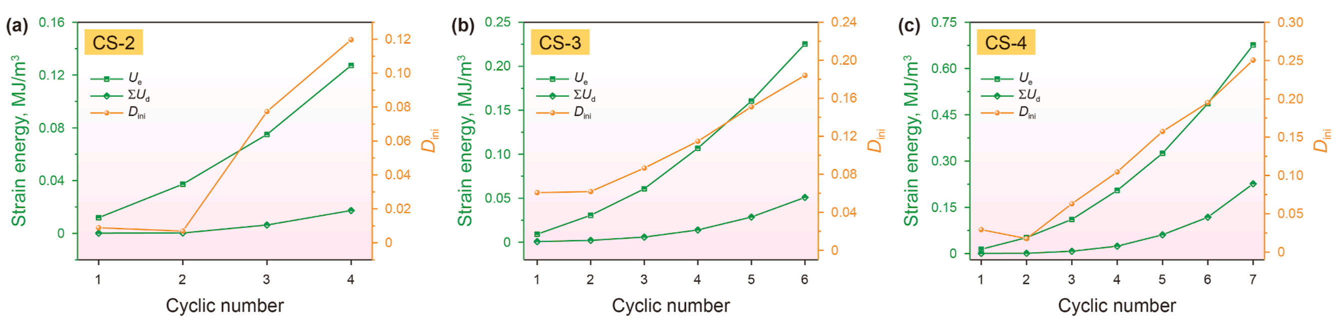

Fig. 3. Evolution of the strain energy and D_{ini} of coal under initial damage loading paths. **(a)** CS-2; **(b)** CS-3; **(c)** CS-4.

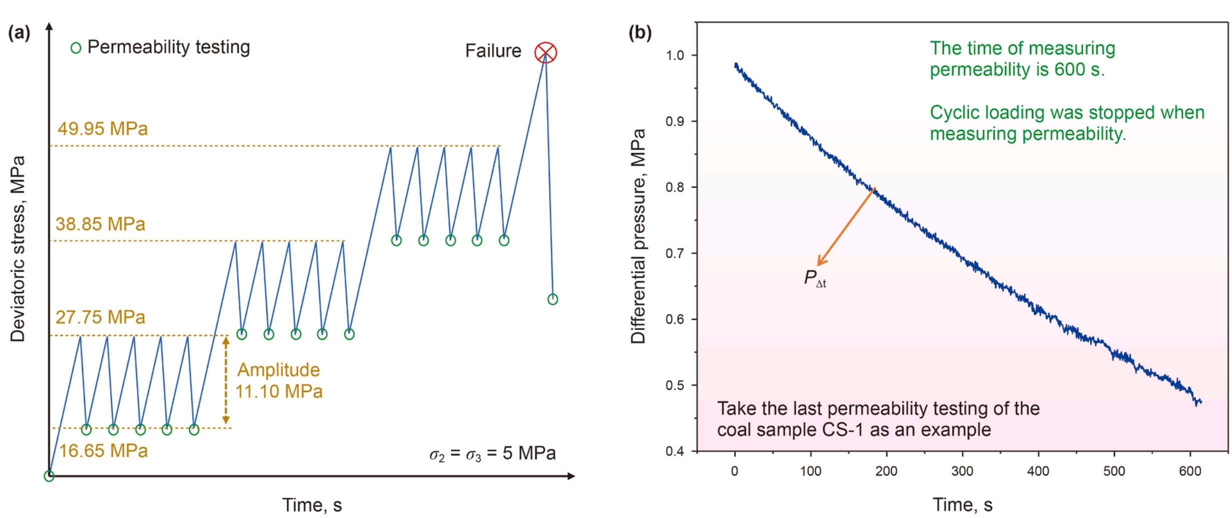

Fig. 4. Experimental program and differential pressure curves. **(a)** Schematic of the cyclic loading and unloading path and the permeability test program; **(b)** representative curve of differential pressure.

moment t, s; and P_{0u} and P_{0d} are the initial upstream and downstream pressures, respectively, Pa. To ensure that the dynamic loading did not interfere with the permeability measurement, cyclic loading was applied during each permeability test. Moreover, the time required for each permeability test was maintained at 600 s. A representative curve of the differential pressure decay during the permeability test is shown in Fig. 4(b).

In summary, the experimental program characterized the mechanical behavior and permeability evolution pattern of coal under different IDDs through cyclic loading paths and permeability tests, which provided important support for an in-depth understanding of the deformation failure mechanism of coal in a complex stress field. As shown in Table 1, two groups of experiments were conducted, and the overall trends in the results of the two groups were similar. In Group-1, the D_{ini} values of the CS-1, CS-2, CS-3, and CS-4 samples were 0, 0.120, 0.184, and 0.251, respectively. Therefore, this study focused on selecting the experimental data from Group-1 for a detailed analysis.

3. Results and discussion

3.1. Mechanical properties of coal with different IDDs

3.1.1. Strength and deformation characterization of coal

Fig. 5 shows the stress-strain curves of coal samples under varying IDDs. The peak strengths of coal samples under different IDDs were 58.425, 52.289, 49.406, and 48.175 MPa, respectively, showing a decreasing trend with the increase of IDDs. This indicates that with the growth in both quantity and size of internal microcracks, the coal samples exhibited reduced structural integrity and diminished load-bearing capacity. Meanwhile, when the IDD was greater, the coal samples experienced greater strain before reaching the peak strength for the overall instability failure to occur, implying that the internal microcracks made the samples more plastic during compression. These results suggest that increasing IDDs not only reduced the strength of the coal samples but also caused them to exhibit more significant plasticity characteristics before failure.

As shown in Fig. 5, for all coal specimens, the volumetric strain first increased with deviatoric stress, indicating a volumetric compaction process dominated by the closure of pre-existing pores and microcracks under the combined action of confining pressure and axial loading. As the stress level increased further, the slope of the volumetric strain–stress curves gradually decreased, especially for the IDD coal specimens. This behavior implies that the rate of volumetric compaction is significantly reduced and that a weak tendency of volumetric dilation appears locally, although the total volumetric strain is still governed by compaction due to the relatively high confining pressure.

To further quantify the effect of initial damage on volumetric behaviors, CS-1 and CS-2 coal specimens were taken as representatives. At deviatoric stresses of 16.65, 27.75, 38.85 and

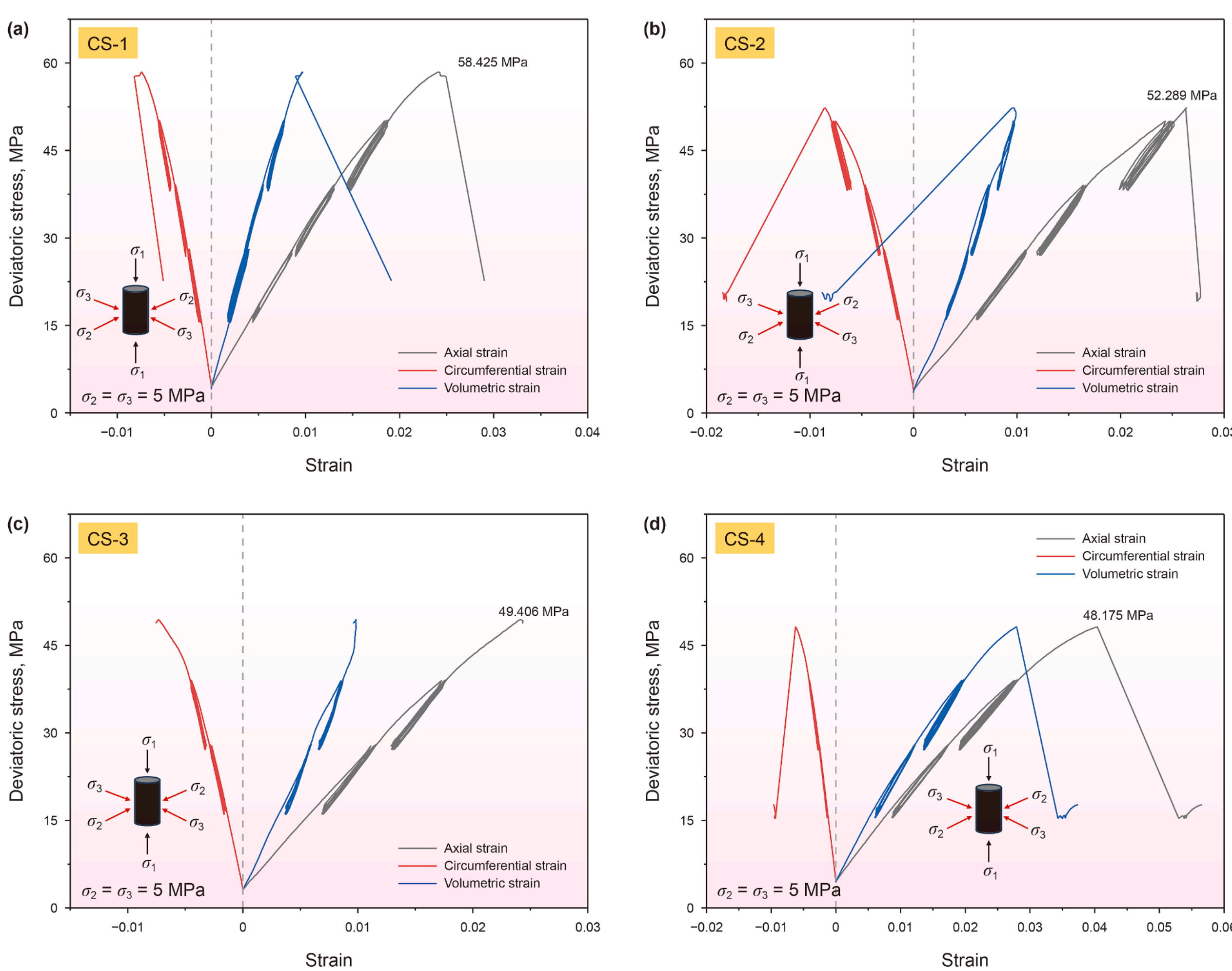

Fig. 5. Stress–strain curves. **(a)** CS-1; **(b)** CS-2; **(c)** CS-3; **(d)** CS-4.

49.95 MPa, the volumetric strains of CS-1 coal specimen were 0.191%, 0.353%, 0.534% and 0.754%, respectively, whereas those of CS-2 coal specimen increased to 0.299%, 0.522%, 0.721% and 0.935%. This confirms that the pre-damaged specimen is more compressible and undergoes larger overall volumetric compaction at a given stress level. This phenomenon can also be found in CS-3 and CS-4 coal samples. To highlight the evolution of the compaction effect, the relative increment of volumetric strain between two successive stress levels is defined as $\Delta\varepsilon_V/\varepsilon_V$. For CS-1 coal specimen, the relative increments between the three loading stages are 0.851, 0.514 and 0.412, while for CS-2 coal specimen, the corresponding values decrease to 0.741, 0.382 and 0.296. Although the total volumetric strain of CS-2 coal specimen is larger, its relative increment attenuates more rapidly with increasing stress. This means that, the closure of pores and microcracks tends to saturate and is increasingly counteracted by the initiation and propagation of new cracks, so that the volumetric response of the damaged coal evolves from strong compaction towards a state of weakened compaction with an incipient dilation tendency at higher stress levels.

In addition, by analyzing the evolution of deformation parameters, the deformation behavior of the coal samples can be understood. In this study, we analyzed the deformation modulus, load–unload response ratio (LURR), and cumulative irreversible strain (Ran et al., 2025a).

Fig. 6 shows the characterization of the deformation parameters of the coal samples in the cyclic stage under different IDDs. The unloading deformation moduli of all the coal samples were usually higher than the loading deformation moduli. The main reason for this is that some of the already activated or propagated microcracks inside the samples closed during stress reduction and showed relatively high stiffness. However, the continuous activation and propagation of microcracks during loading caused the stiffness to decrease significantly. Moreover, the LURR values significantly changed at the beginning of each stress level. These results indicate that as the stress level increases, the further propagation of previously underdeveloped microcracks occurs. In addition, the average deformation moduli of the coal samples with different IDDs were 2.841, 2.527, 2.516, and 1.352 GPa. As the IDD increases, the average deformation modulus decreases. These results further suggest that a higher IDD implies a lower proportion of effective load-bearing units inside the sample, which leads to a decrease in the overall stiffness and deformation resistance. Notably, CS-4 exhibits a markedly lower deformation modulus owing to its relatively high IDD. These results indicate that the greater IDD in sample CS-4 led to a significant weakening of its load-bearing capacity, resulting in high deformation. Furthermore, Fig. 6 shows that with cyclic loading and unloading, there was a certain degree of irreversible strain accumulation, but the IDD had a significant effect on the growth rate of the accumulated irreversible strain. Additionally, the characteristics of the accumulated irreversible strain for the coal samples with different IDDs at stress levels 1 and 2 were 0.296%, 0.385%, 0.574%, and 0.766%, respectively. The samples with higher IDDs exhibited more significant irreversible deformations at lower stresses and with fewer cycles. These outcomes resulted because cracks in the internal structures of these samples are more prone to sliding, propagation, and interpenetration under cyclic stresses, which thereby allows plastic deformation and damage to appear earlier and develop rapidly. These results are consistent with the strength characteristics of the coal samples at high IDDs.

3.1.2. Dissipated energy properties of coal during the cyclic stage

For each loading–unloading cycle, the input energy U_t, elastic energy U_e and dissipated energy U_d were calculated by integrating the stress–strain curves according to Eq. (1). For a given stress

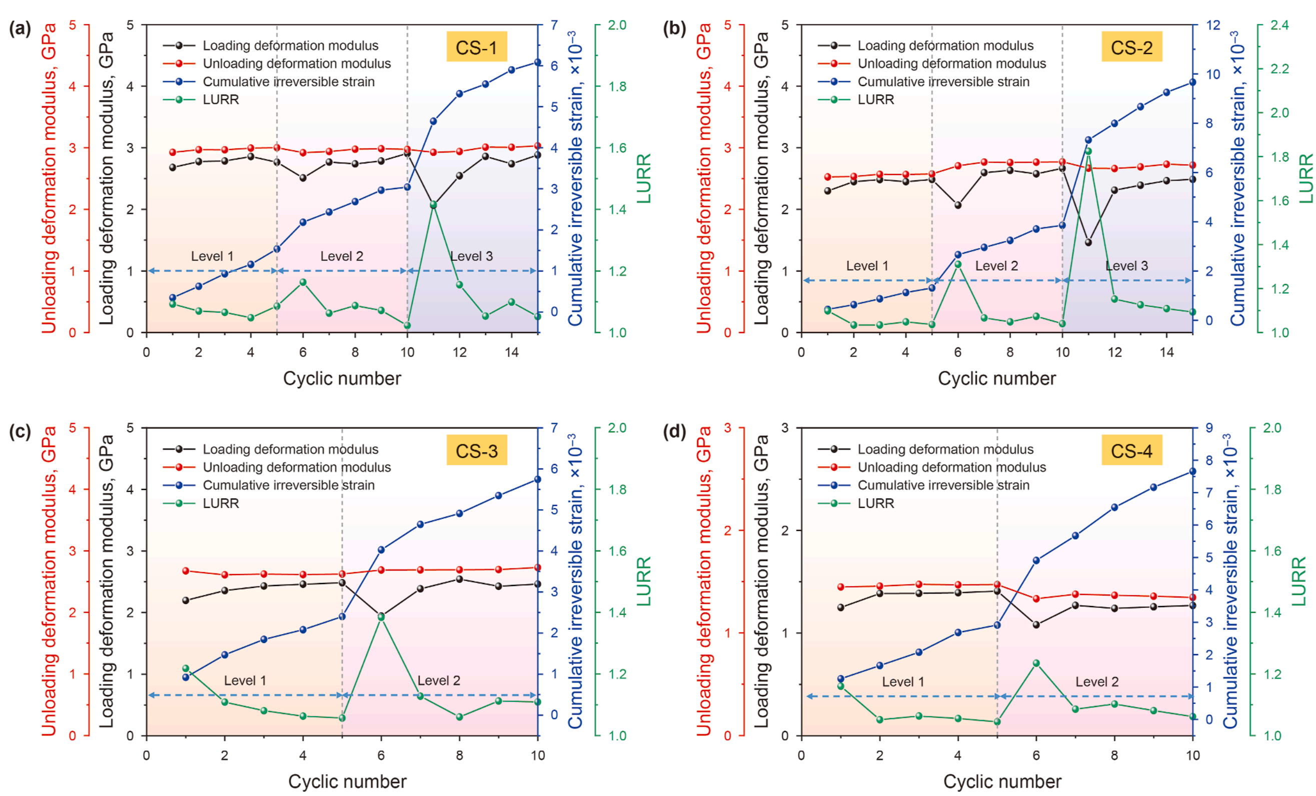

Fig. 6. Evolution of deformation parameters of coal samples in the cyclic stage. **(a)** CS-1; **(b)** CS-2; **(c)** CS-3; **(d)** CS-4.

level, the energy values of all cycles were summed to obtain the cumulative input, elastic and dissipated energies. The energy values plotted in Fig. 7 correspond to the cumulative energies over all cycles at stress levels 1 and 2. With an increase in the IDDs, the strain energy accumulated by coal in the cyclic loading process showed an overall increasing trend, with the growth of dissipated energy being the most significant. Specifically, the dissipated energy at different IDDs were 0.109, 0.139, 0.175, and 0.330 MJ/m^3, respectively. These results indicate that the internal microcracks in samples with higher IDDs are more likely to produce irreversible deformation and localized failure under stress and thus consume more external input energy. The further analysis of the changes in the percentage of dissipated energy (U_d/U_t) revealed that the percentage increased from 9.709% to 11.081%, 13.775%, and 13.820%, respectively, with increasing IDDs. These results indicate that the manner in which the samples utilized the input energy gradually transformed from elastic energy storage to energy dissipation. This significantly increasing trend clearly indicates that a higher IDD results in the coal samples preferring to consume energy in the form of crack propagation with irreversible deformation rather than storing energy in the form of elastic energy. Correspondingly, the average deformation modulus decreased significantly at higher IDDs, further confirming the weakening of the internal load-bearing structure and enhancement of energy dissipation in coal samples with high IDDs.

3.2. Crack characteristics of coal with different IDDs

3.2.1. AE count and crack scale characteristics of coal samples

Fig. 8 shows the evolution characteristics of the AE counts of coal samples with different IDDs during the loading process. For the CS-1 coal samples with $D_{ini} = 0$, the low AE counts at the beginning of the loading indicated that the internal structure was relatively intact and that a higher stress level was required to produce large-scale microcrack activation. In contrast, in coal samples with higher IDDs (particularly CS-4), AE events occurred intensively at lower stresses, indicating that a considerable number of microcracks already existed inside the samples, thus making the local stress concentration effect more significant and crack propagation more easily triggered. This situation led to a notable rise in AE counts during the initial loading phase, and the cumulative AE counts increased rapidly at an earlier stage. In addition, with a further increase in stress, the AE counts of all samples exhibited a significant increasing trend near the peak stress point.

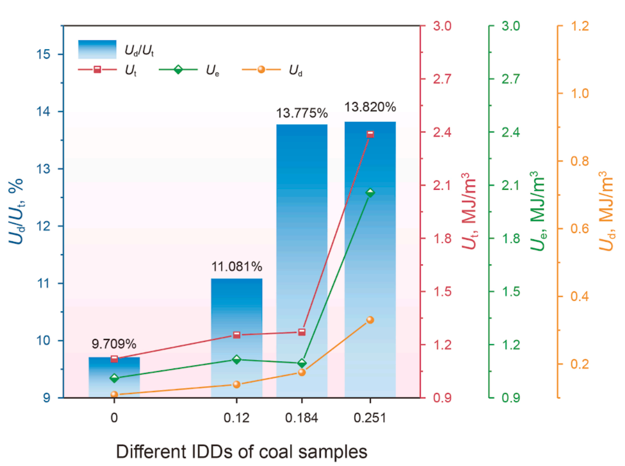

Fig. 7. Cumulative strain energy characterization of coal samples for all cycles at stress levels 1 and 2.

This phenomenon suggests that when the coal samples approached critical instability, many microcracks underwent penetration and violent propagation, releasing a large amount of strain energy that thereby generated a high density of AE events. Overall, a higher IDD resulted in a higher frequency of microcracking activity and damage accumulation in the coal samples at the earlier loading stage, thus confirming that the samples with high IDDs tended to dissipate more energy in the form of microcrack propagation at lower stress levels, which is in line with the revealed strain energy characteristics (Fig. 7).

The b value is essentially a measure of the ratio of small amplitude events to large amplitude events (Ye et al., 2026b; Zhang et al., 2025a). High b values indicate that small-amplitude microcracks are dominant in the coal samples, suggesting that the cracks are of a small scale (Ye et al., 2026c). Conversely, low b values imply a higher number of large-amplitude AE events, indicating that crack distribution is influenced by larger crack propagation. The method for calculating b is as follows (Ran et al., 2025a):

$$\lg N = a - b(A_{dB} / 20), \tag{4}$$

where A_{dB} is the AE amplitude, $A_{dB}/20$ is the magnitude, N is the statistical cumulative frequency of the AE at the magnitude interval, and a is an empirical constant.

The complete AE dataset was input into Eq. (4), using a 4 dB interval to calculate the b value. The evolution patterns of the AE b values for coal samples under different IDDs are shown in Fig. 9. With an increase in the IDDs, the AE b value gradually decreased from approximately 1.863 to 1.389, subsequently decreased to 0.813, and finally decreased to 0.784, showing a continuous decreasing trend. These results indicate that the AE events were dominated by many small-amplitude cracking activities in the samples with lower IDDs. These outcomes resulted from the overall integrity of the coal samples when the IDD was low. The internal cracks were few and small in scale, and the coal samples were mostly in the stages of uniformly distributed microcrack initiation and slow propagation under external loading. As the IDD increased, larger cracks appeared inside the coal samples, and these cracks were more likely to propagate when an external load was applied, thus generating more AE events with higher amplitudes and resulting in a lower b value. The decrease in b value indicates that the proportion of large-scale cracks increased, which is consistent with the previous observation that a higher IDD implies a higher tendency of energy dissipation of the coal samples and a lower deformation modulus.

3.2.2. Characterization of AE energy probability density statistics

The critical index (power law index) serves as a significant parameter in the definition of the power law distribution of a dynamical system (Wu et al., 2016). Moreover, the critical index is influenced by the confusion level of the system and signifies various damage failure mechanisms (Girard et al., 2010; Jiang et al., 2016). The energy values collected for each AE event constitute the energy sample set. The power law distribution function $P(E)$ for this distinct collection of samples is represented as (Sun et al., 2022):

$$P(E) = \frac{E^{-k_p}}{E_{min}^{1-k_p}} E > E_{min}, \tag{5}$$

where E denotes the absolute energy of the AE, aJ; E_{min} is the minimum threshold of the statistical energy, aJ; and k_p refers to the critical index. The value of k_p indicates the probability of the sample appearing as a large-energy AE event. A smaller the critical

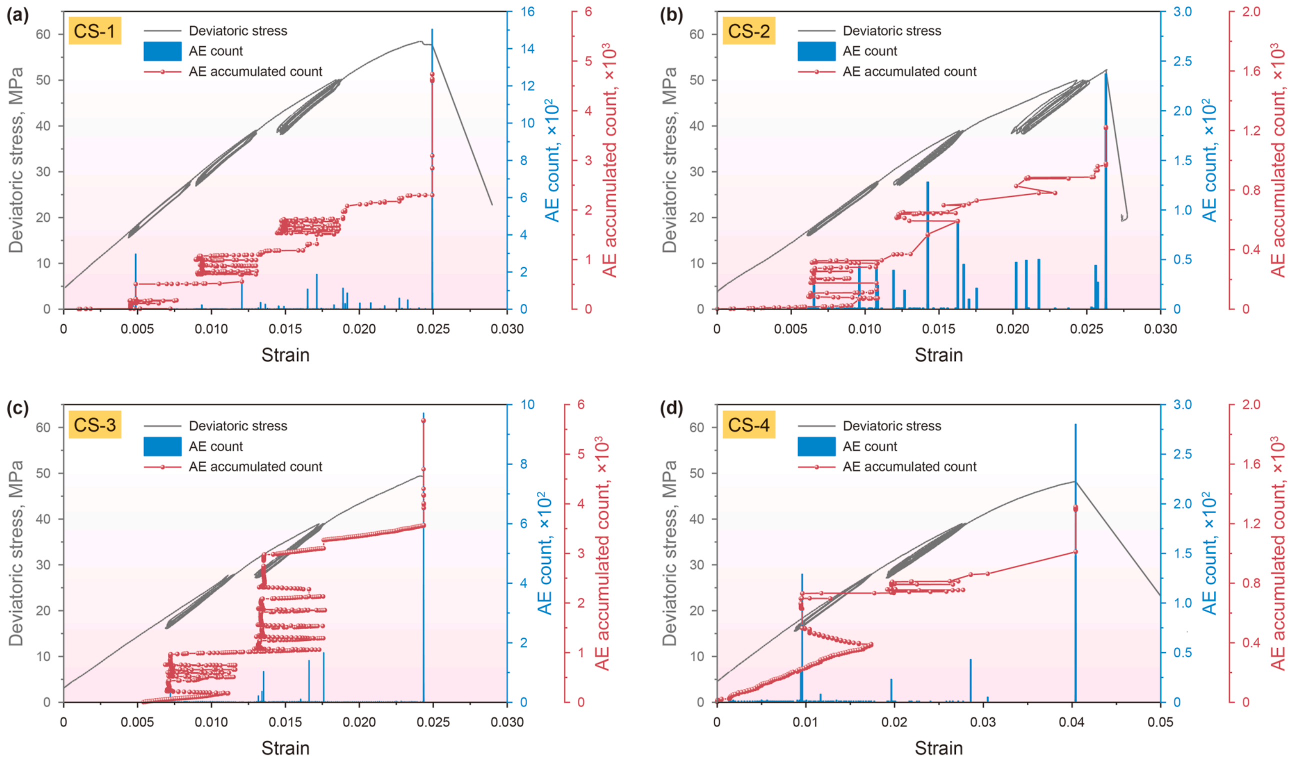

Fig. 8. AE counts evolution at different IDDs. **(a)** CS-1; **(b)** CS-2; **(c)** CS-3; **(d)** CS-4.

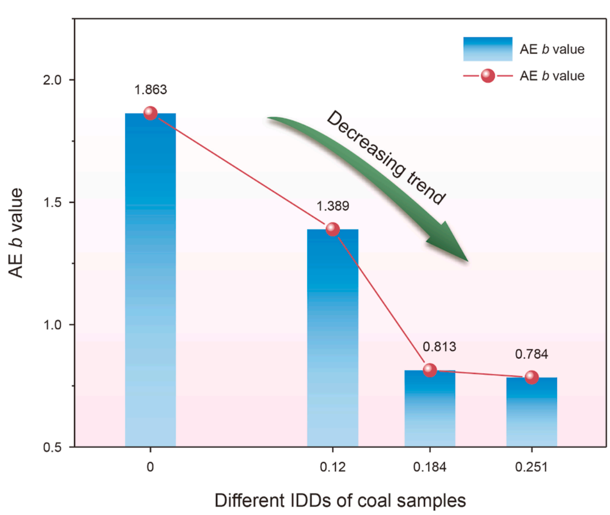

Fig. 9. AE *b* value at different IDDs throughout the experiment.

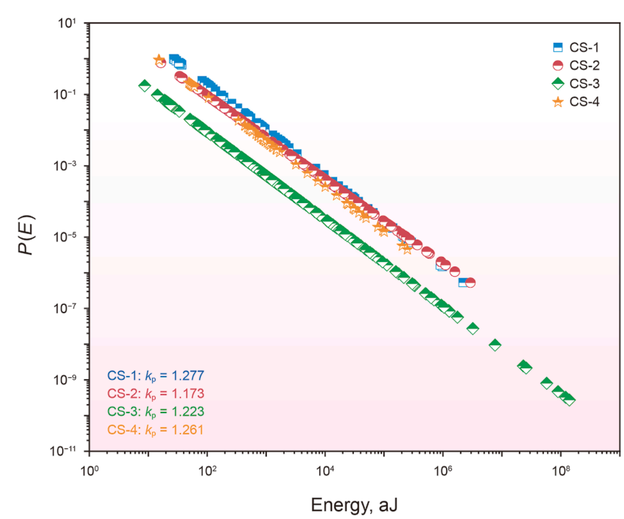

Fig. 10. AE energy probability density characteristics of coal samples at different IDDs.

index indicates a greater energy at which the AE occurs (Sun et al., 2022).

As shown in Fig. 10, the characteristic distribution of the AE energy probability density in logarithmic coordinates exhibits a good linear relationship, indicating that the energy distribution of the entire loading process obeys a power-law distribution. These results indicate that the cyclic failure processes of samples with different IDDs have critical characteristics. Comparing the critical indices of the entire rupture evolution process of samples with different IDDs showed that the critical index of the CS-1 coal sample with $D_{\text{ini}} = 0$ was relatively large. These results suggest that the development of internal cracks in the coal samples had some limitations and that the internal inhomogeneity of the samples was weak, which led to a weakening effect and deterioration of the internal structure of the coal. In contrast, the critical indices of the coal samples with initial damage were smaller than those of the CS-1 coal sample with $D_{\text{ini}} = 0$. These results explain why coal samples with initial damage had an increased possibility of larger energy AE events and why the local yield weakening characteristics were more obvious and thus more likely to lead to the development of internal cracks under compression (Sun et al., 2022). That is, coal samples with initial damage tended to produce a greater percentage of high-energy AE events. This finding supports the overall observation of this study that initial damage makes coal samples favorable for releasing large amounts of energy via crack propagation. This phenomenon was also reflected in the macro-mechanical behavior and strain energy dissipation of coal samples with different IDDs.

3.2.3. Evolution of crack propagation based on AE energy multifractal characteristics

The propagation evolution process of coal cracks exhibits typical nonlinearity and self-similarity, and the AE signals released during the corresponding compressive deformation and rupture processes exhibit obvious multifractal characteristics. The AE absolute energy signal was calculated in this work using the box dimension technique (He et al., 2025b; Ran et al., 2025b), and a multifractal spectrum of the AE absolute energy time series was obtained. The calculation procedure is as follows (Zang et al., 2024):

Let $\{x(t); t = 1, 2, \ldots, N\}$ represent the AE energy time series; after partitioning $\{x(t); t = 1, 2, \ldots, N\}$ into subsequences of length ε_l, the probability measure corresponding to each subsequence $\{P_t(\varepsilon_l)\}$ is given in Eq. (6).

$$P_t(\varepsilon_l) = \frac{N_t}{\sum N_t}, \tag{6}$$

where N_t represents the cumulative value of each partitioned subsequence over different segment lengths, t denotes the total number of subsequences, and $\sum N_t$ indicates the total number of samples.

According to fractal theory, there is a relationship between probability measure $\{P_t(\varepsilon_l)\}$ and measure scale k as follows:

$$\{P_t(\varepsilon_l)\} \propto k^{\alpha} \tag{7}$$

where α represents the singularity scaling index.

Let $N_\alpha(\varepsilon_l)$ denote the number of subsequences associated with the same index α; moreover, the relationship between $N_\alpha(\varepsilon_l)$ and ε_l can be written as follows:

$$N_\alpha(\varepsilon_l) \propto {\varepsilon_l}^{-f(\alpha)} \tag{8}$$

For a given index α, $f(\alpha)$ denotes the dimension of the corresponding fractal subset, and the collection of $f(\alpha)$ over all α constitutes the multifractal spectrum.

A partition function $\chi_q(\varepsilon_l)$ is introduced to characterize the contribution associated with probability measure $\{P_t(\varepsilon_l)\}$:

$$\chi_q(\varepsilon_l) \equiv \sum P_t(\varepsilon_l)^q - {\varepsilon_l}^{\kappa(q)} \tag{9}$$

where q denotes the order of the statistical moment, $-\infty < q < +\infty$. In this work, q is selected within the range [−60, 60], and $\kappa(q)$ denotes the quality index.

$$\kappa(q) = \lim_{\varepsilon_l \to \infty} \frac{\ln \chi_q(\varepsilon_l)}{\ln \varepsilon_l} \tag{10}$$

Eq. (11) is derived via Legendre transformations:

$$\begin{cases} \alpha = \dfrac{\partial(\kappa(q))}{\partial q} \\ f(\alpha) = \alpha(q)q - \kappa(q) \end{cases} \tag{11}$$

On the basis of Eq. (11), the AE signal's multifractal spectrum can be determined.

Among them, $\Delta\alpha$ is defined as follows:

$$\Delta\alpha = \alpha_{\max} - \alpha_{\min}, \tag{12}$$

where $\alpha_{\max}$ denotes the maximum value of the singularity index, $\alpha_{\min}$ represents the minimum value of the singularity index, and $\Delta\alpha$ can reflect the uneven distribution characteristics of the signal. The larger the value of $\Delta\alpha$ is, the larger the signal distribution fluctuation is, corresponding to more obvious multifractal characteristics.

In addition, Δf is defined as follows:

$$\Delta f = f(\alpha_{\max}) - f(\alpha_{\min}), \tag{13}$$

where $f(\alpha_{\max})$ is the value of the fractal dimension at $\alpha = \alpha_{\max}$, $f(\alpha_{\min})$ is the value of the fractal dimension at $\alpha = \alpha_{\min}$, and Δf reflects the probability of occurrence of the subset of large and small measures, with a larger Δf value indicating the predominance of large rupture scale events and a smaller Δf value indicating the predominance of small rupture scale signals.

Fig. 11(a) illustrates the multifractal spectrum of AE absolute energy corresponding to coal specimens with varying IDDs. The AE absolute energy distribution of the coal samples exhibits a complex trend of multifractal characteristics. The overall shapes of the multifractal spectrum of coal samples with varying IDDs were the same, and $f(\alpha)$ showed the change process of increasing and then decreasing with the increase of α, which indicated that the failure processes of the coal samples were similar. However, there were differences in the opening sizes of the multifractal spectrum widths, indicating that the microscopic rupture characteristics of the different coal samples were different. Thus, to further quantify the propagation of cracks in coal samples with different IDDs, Fig. 11(b) shows the variation characteristics of $\Delta\alpha$ and Δf in coal samples. The CS-1 coal sample with $D_{\text{ini}} = 0$ had the smallest $\Delta\alpha$. Overall, $\Delta\alpha$ showed an increasing trend with the increase of the IDDs. These results indicate that the AE energy release was more heterogeneous and complex in samples with higher IDDs. The high IDD provided conditions for the early formation and rapid propagation of the internal crack network, which resulted in AE signals showing stronger multi-scale energy release characteristics. Moreover, the trend of Δf showed that the large crack scale events occupied a more significant position in the high IDD condition. The CS-1 coal sample with $D_{\text{ini}} = 0$ had the lowest Δf. The overall trend of Δf increased with the increase of the IDDs, indicating that the AE signal was more inclined to be dominated by larger energy release events in these samples. These results suggest that a higher IDD implies richer internal micro-existing cracks and that the crack propagation under subsequent stress loading was more likely to form larger-scale failure units and thereby lead to an elevated proportion of high-energy AE events. This complex energy release feature is consistent with previously observed results, such as the strain energy dissipation features and the evolution of the AE b value.

Synthesizing the results of various AE data analyses, the coal samples exhibited a clear trend of microcrack activation and propagation as the IDD increased. Specifically, higher IDDs noticeably elevated AE event frequency at lower stress levels and reduced the AE b value, suggesting a higher ratio of high-energy cracking occurrences. The power law fitting of the AE energy probability density further verified that samples with initial damage were more prone to producing high-energy AE events. In addition, the AE multifractal analysis showed that the energy release of coal samples under high-IDD conditions presented more complex and uneven distribution characteristics. Overall, the AE data analysis revealed the significant influence of the initial damage on the crack propagation process of the coal samples and its energy release mechanism, which provides a powerful dynamic monitoring basis for understanding the failure evolution of coal samples with different IDDs under cyclic loading.

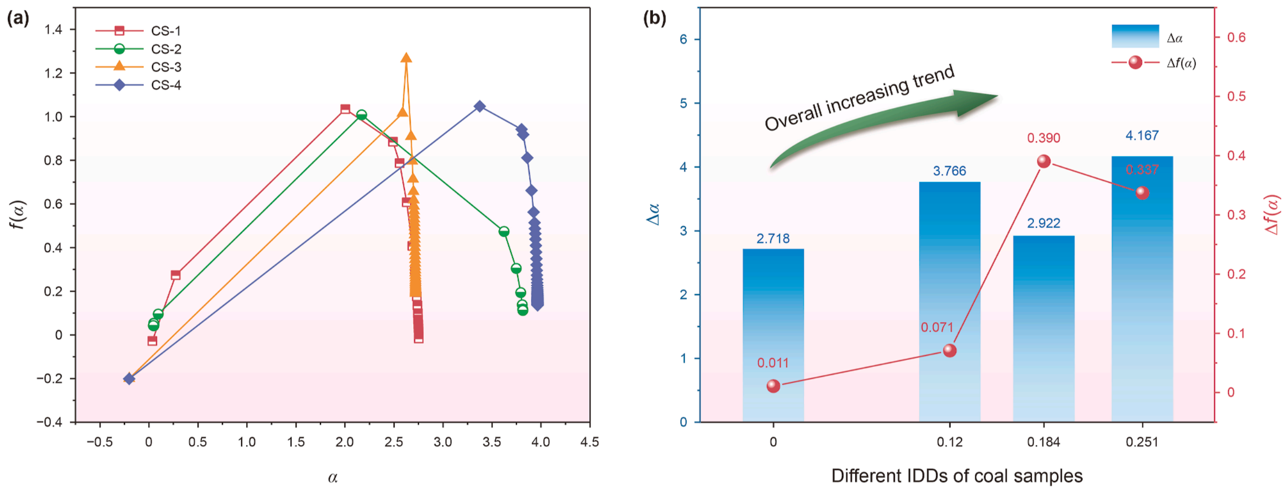

Fig. 11. AE absolute energy multifractal features. **(a)** Multifractal spectrum; **(b)** evolution of $\Delta\alpha$ and Δf.

3.3. Permeability characteristics of coal with different IDDs

3.3.1. Permeability characteristics of coal samples

The permeability evolution under different IDDs was calculated using Eq. (3), as shown in Fig. 12. Overall, all the samples showed a decreasing trend in permeability with increasing stress levels in the cyclic stage. These results were consistent with the findings of Li et al. (2018). The main reason for these results is that under the continuous application of circumferential pressure and increasing axial stress, the coal remained compressed, leading to the constant contraction and compression of the internal primary pores and cracks. Consequently, the gas flow channels became narrow and reduced, thus decreasing the permeability. However, when the IDD was high, the permeability tended to decrease with increasing stress levels. These results indicate that the effect of crack closure inside the samples with high IDDs was relatively weak, whereas the effect of crack propagation was relatively strong. That is, although the pores and cracks in the coal samples with high IDDs were partially compacted during compression, new cracks were also activated or propagated, thus offsetting part of the decrease in permeability owing to compression. Similar to the results of Yang et al. (2019), the permeability tended to decrease within the same stress level. However, the decrease before the arrival of the critical stress level of failure (meaning peak stress) was significantly reduced and even stabilized. This phenomenon highlights the complex process of microcrack propagation and the reorganization of the pore structure inside the coal samples. Under an external load, coal undergoes irreversible deformation, and new cracks are continuously generated. Thus, a further decrease in permeability is inhibited. This effect was particularly prominent in coal samples with high IDDs, indicating that the crack propagation effect was more significant.

In addition, once the stress approaches the peak strength, macroscopic failure occurs immediately, and large-scale penetrating cracks form instantaneously, which drastically increases the fluid transport channels inside the coal samples and results in a significant increase in permeability. For the CS-1 coal sample with $D_{\text{ini}} = 0$, the permeability was always maintained at a low level before failure, and the leap occurred only at the instant of the large-scale penetration of cracks. However, for the coal samples with high IDDs, owing to the existence of many potential cracks, these cracks penetrated in concert with each other under the peak stress to form a more centralized and effective fluid flow network, which led to a more drastic increase in the permeability. This phenomenon further illustrates the sensitivity and vulnerability of coal samples with high IDDs at the critical stress level. Once penetration rupture occurs, the formation of permeable channels is more rapid and concentrated, which strongly affects the permeability.

To more intuitively show the increase in permeability (I_k) under different IDDs after coal failure, the maximum permeability ($k_{\max}$) after failure was compared with the initial permeability (k_{ini}) at the permeability measurement point zero when the coal samples were not loaded, and the increase in amplitude was calculated. The results, as shown in Fig. 13, show that the permeability increase amplitudes of the coal samples under different IDDs were 62.124%, 135.748%, 158.913%, and 194.982%, respectively, showing a trend of a significant increase with the increase in the IDDs. This pattern indicates that the higher the IDD, the richer and more concentrated the through-crack network formed during the final failure of the coal samples, which substantially improved the fluid transport efficiency inside the coal samples. That is, the microcracks in the coal samples with high IDDs were more likely to propagate and connect to macroscopic flow channels when approaching and reaching the peak failure strength, resulting in a more drastic jump in permeability after damage.

3.3.2. Characterization of permeability changing rate

To investigate the effects of cyclic loading and unloading on coal permeability, the absolute permeability change rate (APCR) and relative permeability change rate (RPCR) were introduced in this study (Wang et al., 2025). The specific calculation for APCR is as follows:

$$D_{k_i} = \frac{k_l - k_i}{k_l} \times 100\%, \tag{14}$$

where k_l is the permeability at the first start of loading, mD; and the value of k_{ini} was substituted in this study. Here, k_i is the permeability at the end of the unloading of the i^{th} cycle, mD; and D_{k_i} is the APCR of the coal samples of the i^{th} cycle.

The specific calculation for RPCR is as follows:

$$D_{r_i} = \frac{k_i - k_{i+1}}{k_i} \times 100\%, \tag{15}$$

where k_i is the permeability at the end of the unloading of the i^{th} cycle, mD; k_{i+1} is the permeability at the end of the unloading of

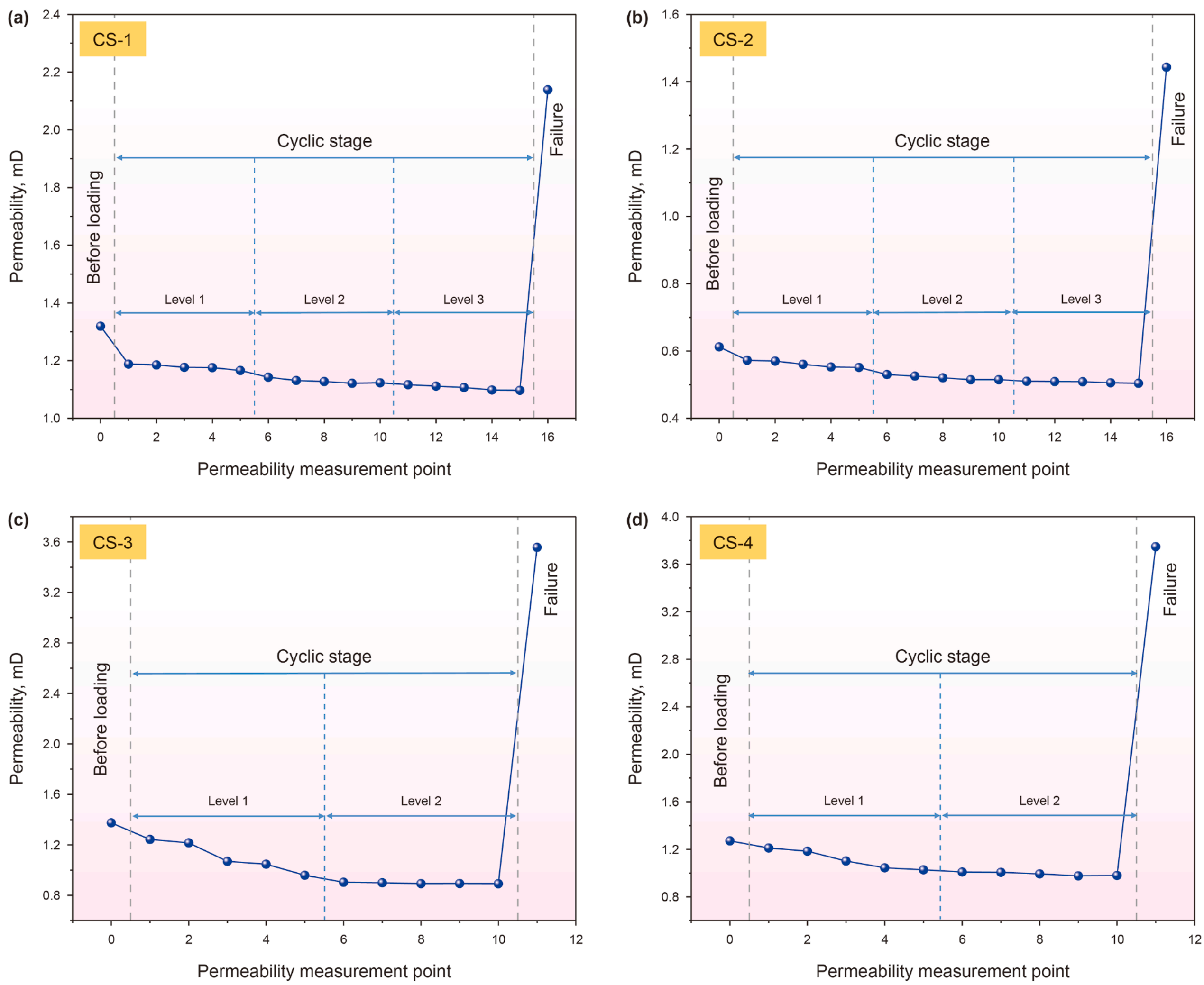

Fig. 12. Permeability evolution of coal samples with different IDDs. **(a)** CS-1; **(b)** CS-2; **(c)** CS-3; **(d)** CS-4.

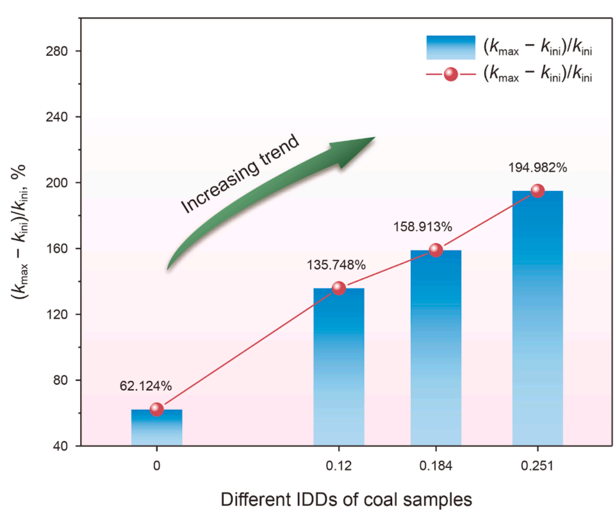

Fig. 13. Increasing amplitude in permeability after failure for coal samples with different IDDs.

the $(i+1)^{\text{th}}$ cycle, mD; and D_{r_i} is the RPCR of the coal samples of the i^{th} cycle.

The APCR was used to measure the absolute damage degree of the permeability of the coal samples during cyclic loading from the initial state. When the APCR increases, it indicates that the permeability of the coal samples was more affected by the compaction effect relative to the initial condition. The RPCR is used to measure the direction and degree of permeability changes in different states within the cyclic stage. When the RPCR is positive, it indicates that the coal samples are in a compaction-dominated state. When RPCR is negative, it indicates that the cracks are open and the channels are increased, which increases the permeability relative to the previous state.

As shown in Fig. 14, the APCR and RPCR of the coal samples exhibited significant differences and dynamic trends during cyclic loading under different IDDs. At lower stress levels, the overall compaction effect of the coal samples was still dominated by the APCR value, which indicated that the APCR value continued to increase or remained high, whereas the RPCR was mostly positive or fluctuated within a small range. These results imply that the

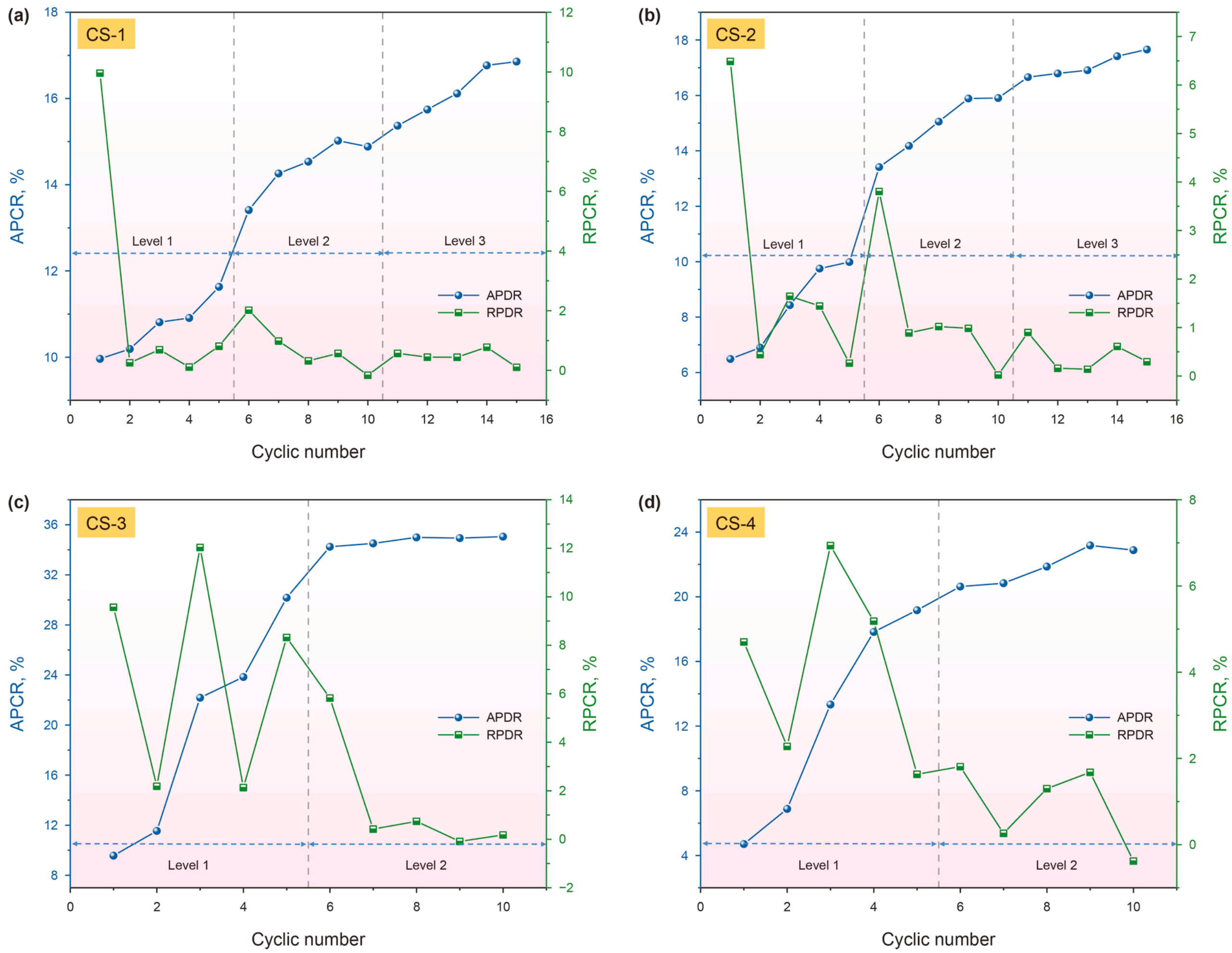

Fig. 14. APCR and RPCR evolution of coal samples with different IDDs. **(a)** CS-1; **(b)** CS-2; **(c)** CS-3; **(d)** CS-4.

coal interior was dominated by the compaction of cracks and that the fluid channels were constantly shrinking. However, as the stress level was further elevated, especially in samples with high IDDs, the internal pre-existing microcracks were continuously activated and expanded under cyclic stress. This process enhanced the crack propagation effect in the localized regions, which led to a negative RPCR at some stages and resulted in a significant decrease in the growth trend of the APCR or a stage-by-stage decrease in the APCR. This phenomenon suggests that the crack propagation effect of samples with high IDDs manifests gradually. This is also consistent with the rapid decay of the relative increment in volumetric strain described in Section 3.1.1. Overall, the higher the IDD, the more complex the internal structure of the coal samples, and the more easily their crack propagation phenomena were stimulated during the cyclic loading process, which led to more frequent and drastic changes in the APCR and RPCR. That is, coal samples with high IDDs were more prone to localized propagation effects under specific stress conditions such that the decreasing trend in permeability could be offset or alleviated locally.

The combined permeability test results showed that for coal sample CS-1 at the highest stress level, the RPCR stabilized after the initial increase in the APCR. These results indicate that the permeability of the coal samples under these conditions was mainly controlled by compaction effects. Although localized crack propagation was present, it only partially counteracted the compaction effect and did not produce a significant increase in the overall permeability. In contrast, although samples with high IDDs showed significant localized crack propagation, no significant increase in permeability was observed before macroscopic failure. These results suggest that under the current experimental conditions, the evolution of permeability was a result of the combined effect of compaction and local crack propagation. The larger the IDD, the easier it is for the internal crack network of the coal to form a localized propagation effect, allowing it to partially offset the compaction-induced decrease in permeability. It was not until the formation of penetrating cracks at the time of failure that a significant jump in permeability occurred.

3.4. Post-failure internal crack characteristics of coal with different IDDs

3.4.1. Internal crack characterization of coal based on the CT scanning

For CT image processing, all scans were exported as grayscale images. In these images, air-filled cracks exhibit very low greyscale values, whereas the coal matrix appears as relatively high greyscale values. Prior to segmentation, a non-local means filter was applied to reduce noise while preserving edge information. For each specimen, the greyscale histogram of the CT slices shows a clear bimodal distribution, with one peak corresponding to the crack phase and the other to the coal matrix. The valley point of the bimodal histogram was chosen as the threshold in Avizo, and then slightly adjusted by visual inspection to ensure that visible cracks were completely included while avoiding over-segmentation of the matrix. Voxels with greyscale values lower than the threshold were classified as cracks, and those higher than the threshold were classified as the coal matrix. Because of the differences between specimens, a separate threshold was determined for each sample rather than using a single global value.

Fig. 15 shows the crack characteristics of coal samples at different IDDs based on CT scanning. Using the slicing method, horizontal and vertical slices of different depths (25%, 50%, and 75%) were obtained. For coal samples with $D_{\mathrm{ini}} = 0$, the cracks in the horizontal slices were relatively sparse and small in scale; however, with an increase in the IDDs, the number of cracks in the horizontal section increased significantly, the scale increased, and they were interconnected to form a more complex crack network. These results suggest that coal samples with high IDDs present more complex and diversified crack networks after failure. This trend can also be seen in the vertical section, where the number of vertical cracks in the samples with $D_{\mathrm{ini}} = 0$ was limited, and the sizes of the cracks were small, whereas the size of the penetrating cracks in samples with higher IDDs was clearly significantly larger. These results indicate that the higher the IDD, the more likely it is for the cracks to propagate and connect and thus form large-scale penetration channels.

Furthermore, the internal cracks in coal samples were visualized using a three-dimensional (3D) reconstruction technique. The number of CT slices used for 3D crack reconstruction was approximately 200 per sample. As shown in Fig. 16(a), threshold segmentation was performed using the top-hat algorithm to distinguish cracks from the matrix (Zou et al., 2023). As shown in Fig. 16(b), a threshold-based segmentation result was randomly selected to verify the reliability of the algorithmic segmentation. The extracted cracks agree well with the actual crack pattern, indicating that the algorithm developed in this study is sufficiently accurate for quantifying the crack volume fraction and its 3D fractal characteristics. Crack segmentation was performed using the Avizo software, and the crack volume percentage (K_{c}) was calculated after segmentation, as shown in Fig. 16(b). In addition, owing to the complexity of the crack morphology, a box-counting method was used to calculate the 3D fractal dimension (D_{CT}). The results showed that the cracks in the coal samples with $D_{\mathrm{ini}} = 0$ were sporadically distributed, whereas the number of cracks in the samples with high IDDs increased dramatically, and the cracks were widely connected and intersected with each other, constituting a larger and more complex 3D crack network, as shown in Fig. 16(c). This complex 3D structure significantly affected the permeability of the coal samples on a macroscopic scale. On this basis, Fig. 16(d) quantitatively analyzes the crack characteristics. For samples with low IDDs to samples with high IDDs, the crack volume percentages were 2.821%, 5.205%, 6.109%, and 8.968%, respectively, showing an increasing trend with an increase in IDDs. These results indicate that the samples with higher IDDs are more likely to form a wider crack network after failure. When the IDD was elevated, the 3D fractal dimension also showed increasing trends of 2.011, 2.039, 2.045, and 2.052. These results indicate that the crack distribution is more complex and multi-scale. These results are consistent with the previous conclusion that the higher the IDD, the easier the propagation of existing cracks, which results in the formation of a larger and more complex crack network, thus affecting the seepage characteristics of the coal samples. Although the fractal dimension of the crack network increased marginally, this small change was statistically significant. This phenomenon reflects a significant increase in the complexity and connectivity of the internal crack structure, which has important

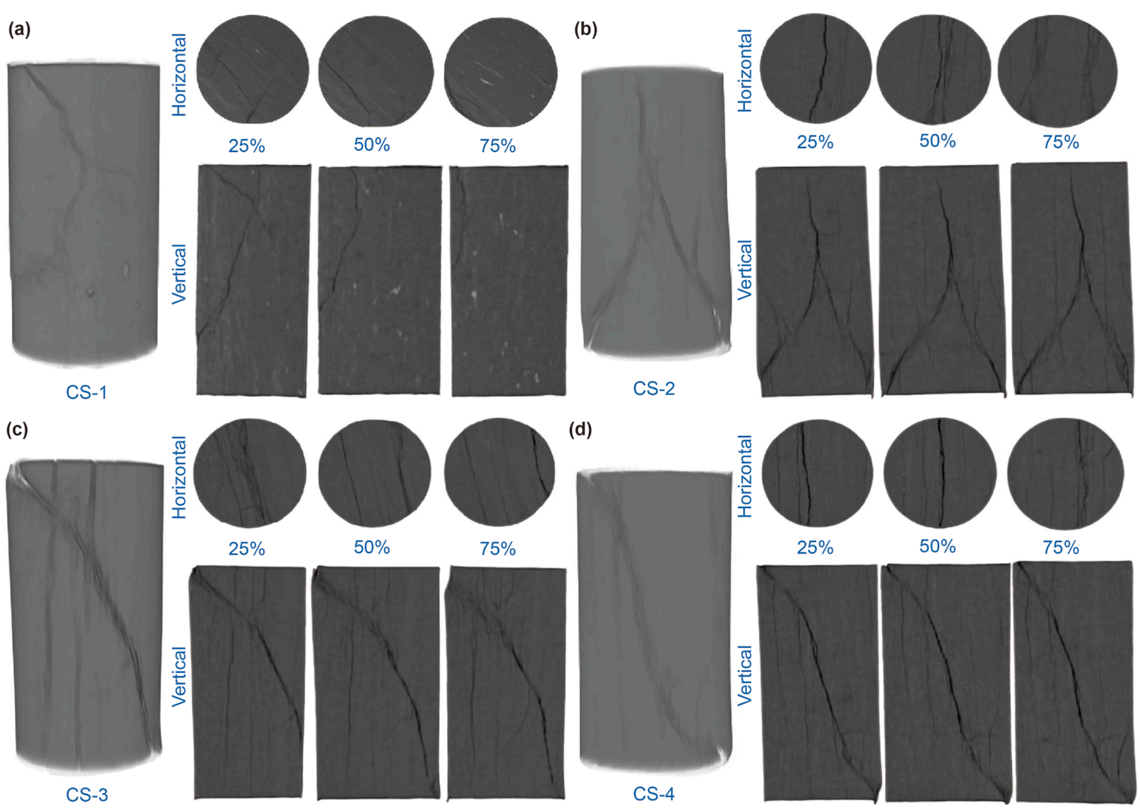

Fig. 15. Crack characteristics of coal samples with different IDDs. **(a)** CS-1; **(b)** CS-2; **(c)** CS-3; **(d)** CS-4.

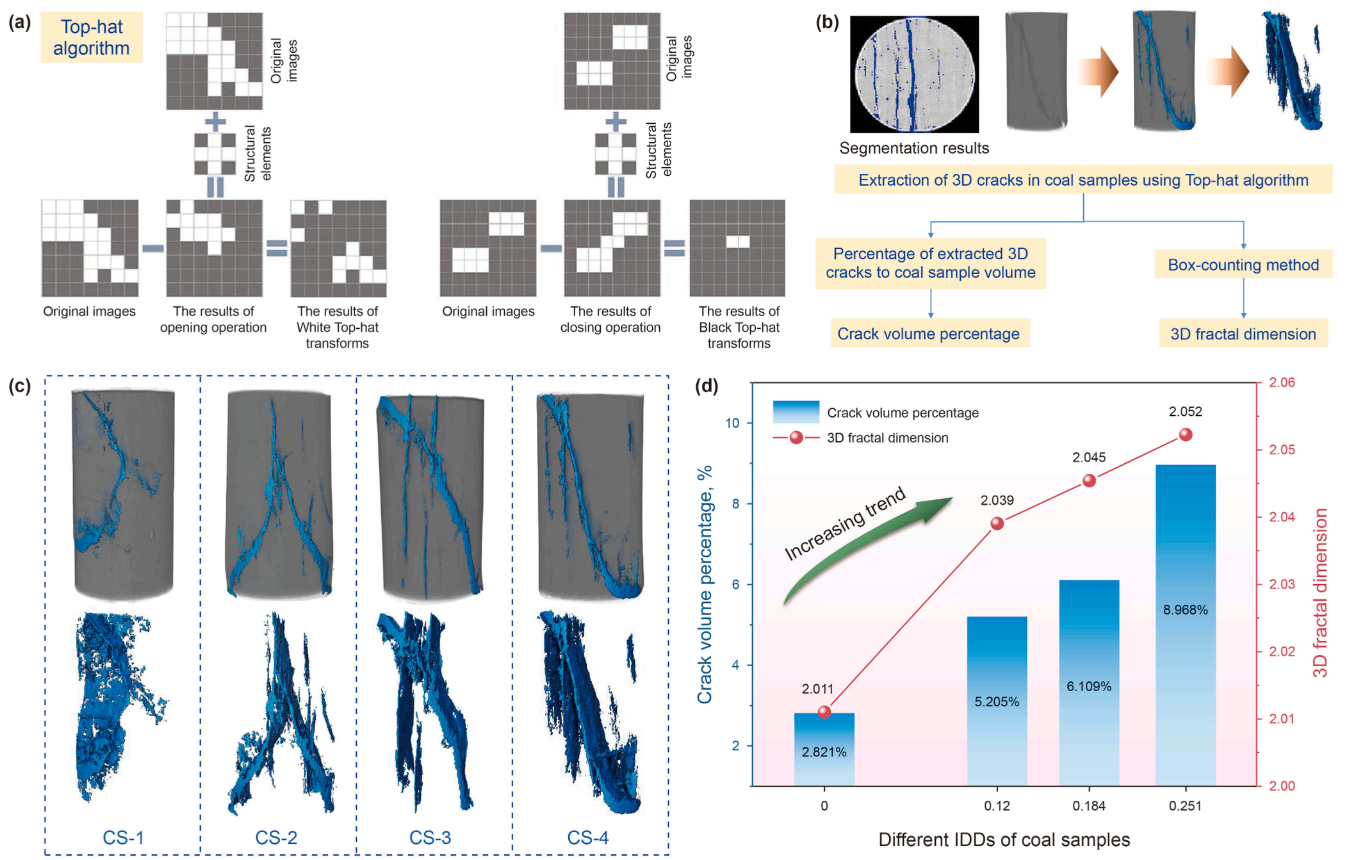

Fig. 16. Quantitative analysis of internal cracks in coal samples with different IDDs. **(a)** Top-hat methods (Zou et al., 2023); **(b)** quantitative analysis methods; **(c)** 3D crack distribution; **(d)** crack volume percentage and 3D fractal dimension.

implications for the crack propagation and permeability evolution of coal samples.

3.4.2. Correlation between AE characteristics and CT crack evolution

To bridge the gap between AE monitoring and post-failure crack structure, a correlation analysis was conducted between the AE-derived parameters (b value, critical index, $\Delta\alpha$, Δf) and CT-derived crack features (3D fractal dimension, D_{CT}).

From a quantitative perspective, the AE-based indicators of crack size distribution are consistent with the CT-derived crack network characteristics. As the initial damage degree increased from CS-1 to CS-4, the b value of AE amplitude statistics decreased markedly (from 1.863 to 0.784), and the critical index of the AE energy power-law distribution also decreased. Meanwhile, $\Delta\alpha$ and Δf both increased, indicating that the AE energy release became more heterogeneous and that large-energy events associated with larger-scale cracks became more dominant. These dynamic AE features correspond well to the post-failure CT observations: the crack volume percentage increased from 2.821% to 8.968%, and the 3D fractal dimension increased from 2.011 to 2.052 as the IDD increased, demonstrating that the internal crack network evolves towards a denser and more complex multi-scale structure.

Additionally, the CT-based fractal dimension (D_{CT}) showed a positive correlation with the multifractal width $\Delta\alpha$ and Δf from AE analysis ($R^2 > 0.65$), as shown in Fig. 17, reinforcing that the complexity of crack growth captured by AE signals is reflected in the final crack morphology. This multi-physics correlation confirms that AE energy distributions can effectively predict crack propagation intensity and spatial complexity.

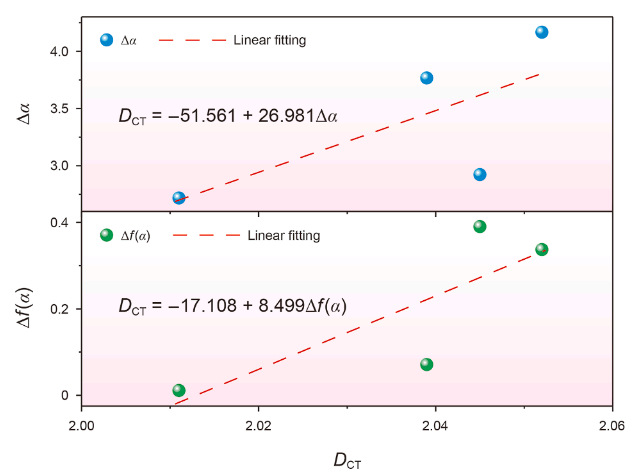

Fig. 17. The correlation characteristics between the CT fractal dimension and the AE multifractal spectrum features.

3.4.3. Correlation between permeability and CT crack characteristics

To quantitatively assess whether the CT-derived crack parameters can reflect the permeability behavior, a regression analysis was conducted between the post-failure permeability enhancement I_k (Fig. 13) and the crack volume percentage K_c as well as the 3D fractal dimension D_{CT} (Fig. 16) for coal specimens.

Fig. 18 shows the scatter plots and linear regression lines of I_k versus K_c and D_{CT}. The correlations are very strong and the slopes

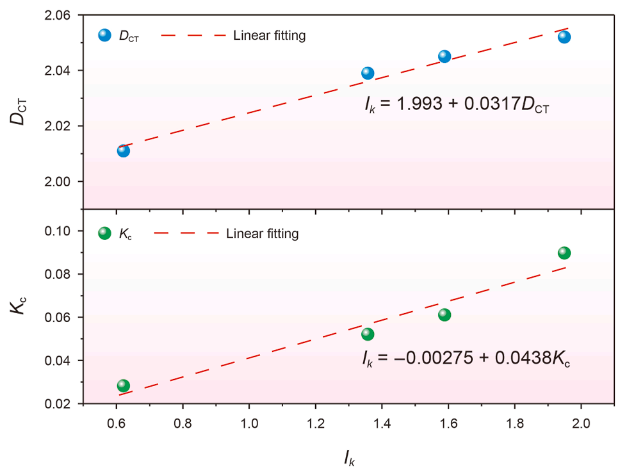

Fig. 18. The correlation characteristics between I_k and K_c as well as D_{CT}.

are positive in both cases, indicating that specimens with larger crack volume fractions and higher 3D fractal dimensions tend to exhibit larger post-failure permeability enhancement. These results demonstrate that the CT-imaged crack network, quantified by crack volume percentage and 3D fractal dimension, can to a considerable extent reflect the permeability response of coal. In particular, the more developed and more complex crack networks revealed by CT provide more efficient flow pathways, which is consistent with the observed larger permeability jumps at failure for high IDD coal samples.

Microscopically, permeability evolution is governed by the competition between crack closure and pore compaction, and stress-induced crack reactivation and propagation. For coal samples with high IDDs, an interesting phenomenon was observed: permeability first decreased with increasing stress, and then exhibited a slight rebound or stabilization in the high-stress stage. In this stage, although part of the crack network is still compressed, newly generated cracks locally increase the connected crack volume and create more direct flow channels. This competition between continued closure of older cracks and opening of new, stress-induced cracks results in a marked attenuation of the permeability reduction rate and even a temporary recovery of permeability at high stress levels. Consistently, the APCR curves of high IDD specimens start to plateau and the RPCR becomes negative (Fig. 14), indicating that the crack propagation effect begins to offset the compaction effect. The post-failure CT results support this interpretation. Regression analysis shows a strong positive correlation between the I_k and K_c as well as D_{CT} (Fig. 18), implying increase in connected crack volume directly translates into a larger permeability jump. Therefore, the permeability recovery observed before macroscopic failure in high IDD specimens can be regarded as the early manifestation of this microstructural transition.

3.5. Mechanisms of crack propagation and permeability evolution

As shown in Fig. 19, this study integrated the mechanical response, AE characteristics, permeability evolution, and CT quantification results to provide an in-depth analysis of coal samples with different IDDs in terms of crack evolution and permeability change. The results show that the IDD has a decisive influence on the crack propagation behavior and permeability change of the coal samples during the loading process.

When the IDD was low, there were fewer cracks inside the coal samples and the entire sample was relatively dense. Under external loading, the compaction effect of the dense closure of microcracks mainly manifested in the early stage, leading to a continuous decrease in permeability with increasing stress. Moreover, the AE results under low IDD conditions also showed that the proportion of energy in the form of elastic energy storage was high, the microcracks started to activate and penetrate in large quantities only at higher stress levels, the positive effect of crack propagation on permeability was weak, and the samples were still compaction-dominated, reducing the effectiveness of the fluid channel. As the IDD increased, more abundant cracks were observed within the samples. The applied stress could expand some of the cracks at low levels, and the AE counts accumulated rapidly at low stress intervals. Decreasing b values, critical indices, and increasing the $\Delta\alpha$ and Δf values of multifractal spectrum all indicated that the cracks evolved towards larger scales. This crack propagation effect occurred simultaneously with the compaction effect. The compressive stress still causes partial crack closure (compaction effect), which reduces the permeability; however, the activation and propagation of internal cracks increases the size of the permeable channels under a certain stress level, which counteracts or even reverses the decreasing trend of the permeability

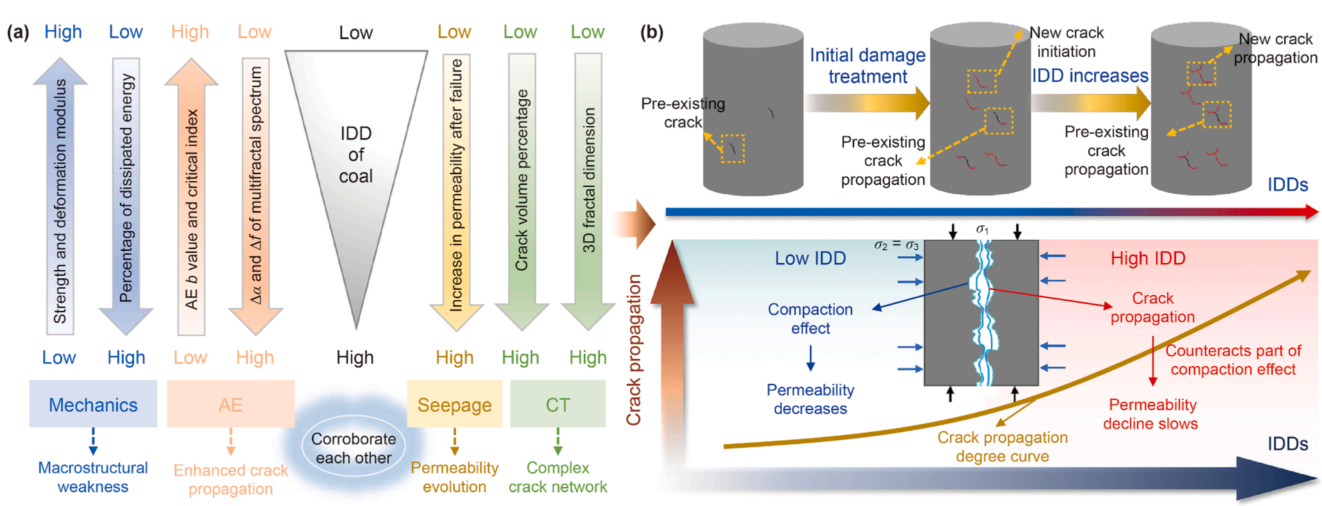

Fig. 19. Mechanism of crack propagation and permeability evolution in coal under the effect of IDDs. **(a)** Experimental results of coal with different IDDs; **(b)** schematic representation of crack propagation of coal with high IDDs.

caused by the compaction (propagation effect). This crack propagation effect is particularly prominent in samples with high IDDs, such that the decrease in permeability slows significantly and even stabilizes near failure.

Furthermore, the AE results revealed the crack initiation and propagation during the loading process from the perspective of dynamic monitoring. When the IDD was larger, the AE events appeared intensively at lower stress levels, indicating that the internal crack network was more easily activated, which increased the impact of crack propagation on the internal structure of the coal samples. The permeability evolution results further illustrate the aforementioned mechanism from the perspective of macroscopic flow transport capacity. The larger the IDD, although the stress increase would close some of the cracks, the local compensatory effect on permeability by more microcrack propagation and penetration in the same period began to appear, which was manifested in the alleviation of the permeability declining trend or even reversal before failure. Eventually, when the stress reached its peak and macroscopic failure occurred, large-scale penetration cracks were formed, and the permeability increased significantly; the higher the IDD, the larger the magnitude of the sudden increase. CT scanning and 3D reconstruction analyses provided intuitive evidence of this mechanism. The CT results showed that the crack volume percentage and fractal dimension after failure in samples with high IDDs significantly increased, indicating that the distribution of cracks was more complex and multi-scale. This complex crack network was quickly transformed into an efficient flow channel in the critical state, resulting in a significant increase in permeability and confirming the decisive contribution of crack propagation to permeability evolution.

3.6. Engineering significance and future research perspectives

The findings of this study have several practical implications for petroleum and geoenergy engineering applications involving deep coal seams and other low-permeability reservoirs. In CBM projects, coal seams act as unconventional reservoirs in which gas production or injection-production operations inevitably induce cyclic changes in pore pressure and effective stress. The present results show that coal with higher IDDs exhibits a stronger tendency towards early crack activation, larger permeability enhancement at failure and reduced mechanical strength. This implies that, in field operations, zones with severe initial damage are more likely to develop connected fracture networks and high-permeability pathways under cyclic loading, which is favorable for gas deliverability but may also accelerate local instability and coal fragmentation. Moreover, the AE approach demonstrated in this study offers a potential methodology for real-time crack monitoring, which can be translated into field-scale diagnostics when adapted with downhole tools. The present results indicate that a decrease in b value, a reduction in the critical index and an increase in multifractal spectrum width could serve as dynamic indicators of the development of more connected fracture networks and impending permeability jumps. This provides a conceptual basis for using real-time AE attributes to infer subsurface crack evolution.

Overall, although the experiments in this study were conducted on coal specimens with different IDDs under controlled laboratory conditions, the identified relationships among crack propagation, energy dissipation, permeability evolution and CT-derived fracture geometry provide a useful framework for the geomechanical design, monitoring and risk assessment of CBM recovery, underground gas storage and other deep petroleum and geoenergy engineering projects involving cyclic loading.

Although this study provided comprehensive insights into the evolution of crack propagation and permeability in coal with varying IDDs under cyclic loading, the results were derived under a specific set of experimental conditions. These controlled conditions limit the generalizability of our results.

First, the effect of loading rate was not systematically investigated in this work. Although the experiments were conducted under a fixed loading rate, the effect of loading rate on crack propagation and AE response is worth further discussion. In general, higher loading rates tend to suppress stable crack growth, resulting in more brittle responses, while lower rates promote progressive damage accumulation and more abundant AE signals. In future work, varying loading rates can be incorporated to explore their influence on energy dissipation modes, permeability jumps, and multifractal spectrum shifts. Second, the current study used a fixed confining pressure to simulate in-situ stress conditions. However, deformation and permeability behavior of coal is known to be highly sensitive to confining pressure. Increasing confining pressure generally promotes crack closure, reduces permeability, and delays failure onset. Further studies incorporating multiple confining pressure levels are needed to clarify the pressure dependence of permeability recovery, especially in deep coal seams. Third, the experiments were conducted on standard-size coal specimens, which may not fully capture the heterogeneity and fracture interaction present at field scale. Scale effects influence both the statistical distribution of cracks and the connectivity of crack networks, potentially altering AE event clustering, b value distribution, and permeability trends. Future upscaling efforts, such as numerical modeling or physical similarity simulations at larger scales, will be essential to validate whether the observed AE-permeability-crack relations hold under engineering-scale conditions. Fourth, in this study, CT scanning was only performed for the failure states of the coal samples. While this approach effectively captures the final fracture morphology and helps interpret permeability changes, it does not directly visualize the internal damage states induced by the preloading paths. This is a limitation of the current experimental design. Nevertheless, the initial structural characteristics of coal samples with initial damage were extensively documented in previous studies, it has since been demonstrated that initial damage promotes crack propagation (Yin et al., 2023). Future studies may consider integrating in-situ or staged CT scanning to directly visualize the progressive crack development during preloading. In addition, pairing CT scanning with the AE localization technique could improve this work. Furthermore, the threshold effect of the IDDs can be explored in future work by preparing a larger number of specimens with more finely graded IDDs.

4. Conclusions

In this study, coal samples with different IDDs were prepared, and experiments were carried out under cyclic loading. This work focuses on investigating the effect of IDDs on the crack propagation and permeability evolution of coal and systematically explores the mechanism of its action by combining it with AE monitoring and CT technology. The conclusions of this study are as follows.

(1) Based on the analysis of the AE counts, *b* values, and energy power-law distributions, it was found that the higher the IDD, the easier it was for coal samples to induce more high-energy AE events, significantly reduce the critical index and *b* value, and form larger-scale cracks and destabilize earlier. In addition, the $\Delta\alpha$ and Δf of AE multifractal spectrum increased with the increase of IDDs. The AE results suggest

that pre-existing microcracks accelerate the initiation and growth of larger cracks under cyclic loading.

(2) The permeability evolution was influenced by compaction effects versus local crack propagation effects. In coal samples with low IDDs, compaction dominated, leading to a continuous decline in permeability. In contrast, coal samples with high IDDs exhibited a delayed decrease in permeability owing to partial offsetting by crack propagation. Eventually, the permeability rapidly increased at the time of macroscopic failure of the coal samples. The increase in post-damage permeability was positively correlated with IDD at 62.1%, 135.7%, 158.9%, and 195.0%, respectively.

(3) Additionally, the CT scanning results confirmed that coal samples with high IDDs developed a more extensive and complex crack network with a significantly increased crack volume percentage and 3D fractal dimension. CT scanning results showed crack volume percentage increasing from 2.821% to 8.968% and the 3D fractal dimension from 2.011 to 2.052 as IDDs increased.

(4) With increasing IDDs, the crack propagation effect gradually appeared during the stress loading process, so that the change of permeability presented a more complex dynamic characteristic. Near failure, large-scale penetrating cracks formed and triggered a drastic increase in permeability. The AE data revealed the dynamic process of crack propagation, the permeability results indicated the presence of the crack propagation effect, and the CT scanning, on the other hand, demonstrated the results of the crack propagation effect.

CRediT authorship contribution statement

Qi-Can Ran: Writing – review & editing, Writing – original draft. **Yun-Pei Liang:** Writing – review & editing. **Chun-Feng Ye:** Methodology. **Teng-Fei Ma:** Investigation. **Zi-Han Chen:** Writing – review & editing.

Data availability

All data used during this research are available from the corresponding author by reasonable request.

Declaration of interest statement

The authors declare that they have no known competing financial interests or personal relationships that could have appeared to influence the work reported in this paper.

Acknowledgements

This work was financially supported by the National Natural Science Foundation of China (Grant No. 52174166), and Opening Project of State Key Laboratory of Coal Mine Disaster Dynamics and Control, Chongqing University (Grant No. 2011DA105287-FW202602), which were gratefully acknowledged. The authors would like to thank Prof. Quan-Le Zou and Ms. Jun-Hui Mu from Chongqing University for the useful discussion in this work. Besides, the authors would like to thank Dr. Yang Liu and Dr. Zhao-Peng Zhang from the Key Laboratory of Deep Earth Science and Engineering (Ministry of Education) at Sichuan University for their useful discussion and experiment assistance in this work.

References

Chen, Z.H., Zou, Q.L., Lv, F.X., et al., 2025. Quantitative characterization of fracture surface undulations and gas-guiding patterns in fractured rocks under steady loading. Int. J. Min. Sci. Technol. 35 (10), 1753–1773. https://doi.org/10.1016/j.ijmst.2025.08.017.

Cui, Q.Z., Wu, F., Liu, J.F., et al., 2025. A variable fractal-order rock salt creep model with full-time domain memory effect and its application in salt cavern hydrogen storage. Energy 338, 138870. https://doi.org/10.1016/j.energy.2025.138870.

Dai, J.H., Gong, F.Q., He, Z.C., et al., 2024. Quantitative estimation method for the excavation-induced weakening effect of rock mass parameters in deep tunnels. Eng. Geol. 330, 107416. https://doi.org/10.1016/j.enggeo.2024.107416.

Fan, J.Y., Guo, P.Y., Wang, Y.F., et al., 2025. Stability analysis of compressed air energy storage in underground space: A comparative research of coal mine roadway and salt cavern. Geomech. Energy Environ. 43, 100715. https://doi.org/10.1016/j.gete.2025.100715.

Fan, L., Liu, S.M., 2019. Evaluation of permeability damage for stressed coal with cyclic loading: An experimental study. Int. J. Coal Geol. 216, 103338. https://doi.org/10.1016/j.coal.2019.103338.

Girard, L., Amitrano, D., Weiss, J., 2010. Failure as a critical phenomenon in a progressive damage model. J. Stat. Mech. Theory Exp. 2010 (1), P01013. https://doi.org/10.1088/1742-5468/2010/01/P01013.

Guo, J.N., Liu, J.F., Li, Q., et al., 2019. Variation law of coal permeability under cyclic loading and unloading. Therm. Sci. 23 (3 Part A), 1487–1494. https://doi.org/10.2298/tsci180907215g.

Guo, S., He, M.C., Jeon, S., 2025a. Visualization test and numerical simulations of 2D blasting crack propagation. J. Rock Mech. Geotech. Eng. 17 (8), 4871–4888. https://doi.org/10.1016/j.jrmge.2024.10.013.

Guo, Y.D., Huang, L.Q., Li, X.B., 2025b. Influence of 3D forced water-based working fluid imbibition on dynamic responses of deep anisotropic shale reservoir. Int. J. Rock Mech. Min. Sci. 194, 106195. https://doi.org/10.1016/j.ijrmms.2025.106195.

He, D., Li, S.G., Kong, X.G., et al., 2025a. Mechanism of gas seepage enhancement based on the evolution of micro-pores and energy dissipation in coal under dynamic load. Geomech. Energy Environ. 44, 100762. https://doi.org/10.1016/j.gete.2025.100762.

He, D., Li, S.G., Kong, X.G., et al., 2025b. Effects of dynamic impact on micro-structure evolution and permeability enhancement of coal. Energy Fuel. 39 (23), 11099–11109. https://doi.org/10.1021/acs.energyfuels.5c01419.

He, H.Y., Nie, B.S., Liu, P., et al., 2025c. Functional group-driven modulation of combustion-gas kinetics in underground coal enhanced combustion. Process Saf. Environ. Prot. 200, 107359. https://doi.org/10.1016/j.psep.2025.107359.

He, Z.C., Gong, F.Q., Gao, M.Z., 2025d. Experimental study on the mechanical behavior of high-stress rocks during real-time drilling. Int. J. Coal Sci. Technol. 12 (1), 37. https://doi.org/10.1007/s40789-025-00774-5.

He, Z.C., Gong, F.Q., Li, R., et al., 2025e. Energy relief effect of real-time drilling to prevent rockburst in high-stress rock. J. Rock Mech. Geotech. Eng. 18 (2), 1460–1475. https://doi.org/10.1016/j.jrmge.2025.04.030.

Hou, R.B., Zhang, K., Tao, J., et al., 2019. A nonlinear creep damage coupled model for rock considering the effect of initial damage. Rock Mech. Rock Eng. 52 (5), 1275–1285. https://doi.org/10.1007/s00603-018-1626-7.

Huang, P., Zhang, J.X., Damascene, N.J., et al., 2021a. A fractional order viscoelastic-plastic creep model for coal sample considering initial damage accumulation. Alex. Eng. J. 60 (4), 3921–3930. https://doi.org/10.1016/j.aej.2021.02.054.

Huang, P., Zhang, J.X., Spearing, A.J.S., et al., 2021b. Experimental study of the creep properties of coal considering initial damage. Int. J. Rock Mech. Min. Sci. 139, 104629. https://doi.org/10.1016/j.ijrmms.2021.104629.

Jiang, C.B., Duan, M.K., Yin, G.Z., et al., 2017. Experimental study on seepage properties, AE characteristics and energy dissipation of coal under tiered cyclic loading. Eng. Geol. 221, 114–123. https://doi.org/10.1016/j.enggeo.2017.03.005.

Jiang, D.Y., Xie, K.N., Jiang, X., et al., 2016. Statistical analysis of acoustic emission energy distribution during uniaxial compression of shale. Chin. J. Rock Mech. Eng. 35 (S2), 3822–3828. https://doi.org/10.13722/j.cnki.jrme.2015.0699.

Jiang, J.Q., Su, G.S., Zhang, X.H., et al., 2020. Effect of initial damage on remotely triggered rockburst in granite: An experimental study. Bull. Eng. Geol. Environ. 79 (6), 3175–3194. https://doi.org/10.1007/s10064-020-01760-8.

Kong, X.G., He, D., Liu, X.F., et al., 2022. Strain characteristics and energy dissipation laws of gas-bearing coal during impact fracture process. Energy 242, 123028. https://doi.org/10.1016/j.energy.2021.123028.

Lei, B., Yu, L.J., Chen, T.Y., et al., 2023. Experimental study on the initial damage and mechanical property evolution of recycled coarse aggregates under freeze–thaw cycles and repeated loads. Constr. Build. Mater. 375, 130972. https://doi.org/10.1016/j.conbuildmat.2023.130972.

Li, C.B., Yang, D.C., Xie, H.P., et al., 2025. Anisotropic fracture evolution and size effect of the fracture process zone in laminated shales derived from digital image correlation. Rock Mech. Rock Eng. 58 (1), 203–224. https://doi.org/10.1007/s00603-024-04209-6.

Li, F., Gao, M.Z., Ye, S.Q., et al., 2023. Formation mechanism of core discing during drilling under deep in-situ stress environment: Numerical simulation and laboratory testing. J. Cent. South Univ. 30 (10), 3303–3321. https://doi.org/10.1007/s11771-023-5465-7.

Li, Q.M., Liang, Y.P., Zou, Q.L., 2018. Seepage and damage evolution characteristics of gas-bearing coal under different cyclic loading–unloading stress paths. Processes 6 (10), 190. https://doi.org/10.3390/pr6100190.

Liang, Y.P., Ran, Q.C., Zou, Q.L., et al., 2022. Experimental study of mechanical behaviors and failure characteristics of coal under true triaxial cyclic loading and unloading and stress rotation. Nat. Resour. Res. 31 (2), 971–991. https://doi.org/10.1007/s11053-022-10022-1.

Liu, C., Zhang, J.H., Wu, S.W., et al., 2024a. Experimental study on permeability evolution of deep high-stressed coal under major horizontal stress unloading paths. Int. J. Min. Sci. Technol. 34 (11), 1495–1508. https://doi.org/10.1016/j.ijmst.2024.10.004.

Liu, H.H., Lin, B.Q., Jiang, C.B., et al., 2023. Sensitivity of coal permeability to multiple stresses. J. Min. Saf. Eng. 40 (4), 818–825. https://doi.org/10.13545/j.cnki.jmse.2022.0664.

Liu, T., Li, M.Y., Lin, B.Q., et al., 2024b. Evolution of coal fractures and its influence on permeability during progressive failure based on in situ CT scanning. Energy Fuel. 38 (15), 14119–14135. https://doi.org/10.1021/acs.energyfuels.4c02404.

Miao, Y.C., Wu, H.K., Bai, K.L., et al., 2024. Mechanical behaviors and damage constitutive model of pre-damaged and saturated granites under uniaxial compression. Bull. Eng. Geol. Environ. 83 (7), 270. https://doi.org/10.1007/s10064-024-03768-w.

Niu, Z.H., Zhu, Z.D., Que, X.C., et al., 2024. Experimental study on damage evolution process, seepage characteristics, and energy response of columnar jointed basalt under true triaxial cyclic loading. Geoenergy Sci. Eng. 237, 212774. https://doi.org/10.1016/j.geoen.2024.212774.

Ran, Q.C., Liang, Y.P., Ye, C.F., et al., 2025a. Mechanical deterioration and crack propagation characteristics of mudstone under cyclic loading: insights from acoustic emission fractal analysis. Rock Mech. Rock Eng. https://doi.org/10.1007/s00603-025-05111-5.

Ran, Q.C., Zhao, W.T., Liang, Y.P., et al., 2025b. Deciphering confining pressure effects on coal failure mechanisms using acoustic emission approaches. Eng. Fract. Mech. 329, 111592. https://doi.org/10.1016/j.engfracmech.2025.111592.

Sun, B., Tang, W.F., Zhen, S., et al., 2022. Statistical analysis of rock acoustic emission energy and waiting time based on self-organized criticality theory. Rock Soil Mech. 43 (9), 2525–2538. https://doi.org/10.16285/j.rsm.2021.1878 (in Chinese).

Taheri, A., Zhang, Y.B., Munoz, H., 2020. Performance of rock crack stress thresholds determination criteria and investigating strength and confining pressure effects. Constr. Build. Mater. 243, 118263. https://doi.org/10.1016/j.conbuildmat.2020.118263.

Wang, C.Y., Zhang, D.M., Tan, D.J., et al., 2024. Study on the evolution of limestone damage and permeability under the tunnel driving stress path. Constr. Build. Mater. 425, 136050. https://doi.org/10.1016/j.conbuildmat.2024.136050.

Wang, C.Z., Zhou, B., Li, S.G., et al., 2026. Dominant governing mechanisms of deformation-seepage and dynamic evolution model of permeability in gas-containing coal under coupled stress-pore pressure. Fuel 404, 136408. https://doi.org/10.1016/j.fuel.2025.136408.

Wang, D.K., Feng, H.H., Wei, J.P., et al., 2025. Analysis of permeability evolution law of gas-bearing coal under cyclic loading condition. Coal Sci. Technol. 53 (S1), 151–164. https://doi.org/10.12438/cst.2023-1893.

Wu, Q.F., Yu, M.G., Zheng, K., et al., 2025a. Influence of ignition positions on the flame behavior of non-uniform methane-air mixture explosions in vertically closed pipes. Process Saf. Environ. Prot. 196, 106872. https://doi.org/10.1016/j.psep.2025.106872.

Wu, S., Ge, H.K., Wang, X.Q., et al., 2025b. Evaluating hydraulic fracturing effectiveness based on the improved connection model of acoustic emission events. Pet. Sci. 22 (10), 4145–4156. https://doi.org/10.1016/j.petsci.2025.07.018.

Wu, X.W., Qin, S.Q., Xue, L., et al., 2016. Physical mechanism of major earthquakes by earthquake cases. Chin. J. Geophys.-Chin. Ed. 59 (10), 3696–3710. https://doi.org/10.6038/cjg20161016.

Xu, L., Gong, F.Q., Dai, J.H., et al., 2025. Effects of bedding angles on rockburst proneness of layered anisotropic phyllites. J. Rock Mech. Geotech. Eng. 17 (7), 4288–4313. https://doi.org/10.1016/j.jrmge.2024.11.012.

Yang, L., Fan, C.J., Luo, M.K., et al., 2025. Geological parameters and gas mixture composition on enhanced coalbed methane recovery: A THM modeling approach. Pet. Sci. 22 (5), 2078–2095. https://doi.org/10.1016/j.petsci.2025.02.002.

Yang, S.Q., Li, H., Yang, Z., et al., 2024. Three-dimensional peridynamic simulation on triaxial compression failure mechanical behavior of cylindrical marble specimen containing pre-existing fissures. Eng. Fract. Mech. 312, 110600. https://doi.org/10.1016/j.engfracmech.2024.110600.

Yang, X.L., Cao, J., Cheng, X.Y., et al., 2019. Mechanical response characteristics and permeability evolution of coal samples under cyclic loading. Energy Sci. Eng. 7 (5), 1588–1604. https://doi.org/10.1002/ese3.368.

Ye, C.F., Chen, H.J., Li, C.B., et al., 2026a. Prediction of continuous–discontinuous failure of granite subjected to direct shearing using acousto-optical-mechanical scheme. J. Rock Mech. Geotech. Eng. https://doi.org/10.1016/j.jrmge.2025.12.018.

Ye, C.F., Li, C.B., Chen, H.J., et al., 2026b. Nonlinear progressive failure mechanism and shear strength model of deeply buried jinping marble under direct shear. Int. J. Rock Mech. Min. Sci. 198, 106380. https://doi.org/10.1016/j.ijrmms.2025.106380.

Ye, C.F., Li, C.B., Chen, H.J., et al., 2026c. Progressive failure mechanism and shear strength model of granite under cyclic direct shear. Rock Mech. Rock Eng. 59 (2), 1455–1482. https://doi.org/10.1007/s00603-025-04962-2.

Yin, D.W., Ding, Y.S., Wang, F., et al., 2023. Experimental study on mechanical properties of coal soaked in pressurized water considering initial damage. J. China Coal Soc. 48 (12), 4417–4432. https://doi.org/10.13225/j.cnki.jccs.2023.0256 (in Chinese).

Yu, W.X., Jin, L., Du, X.L., et al., 2022. Effect of initial damage state on static and dynamic fracture of concrete with different sizes: An experimental study. Eng. Fract. Mech. 274, 108797. https://doi.org/10.1016/j.engfracmech.2022.108797.

Zang, Z.S., Li, Z.H., Gu, Z.J., et al., 2024. The multi-dimensional joint response of the electric potential time–frequency-field in the fracture process of flawed coal under dynamic load. Theor. Appl. Fract. Mech. 131, 104415. https://doi.org/10.1016/j.tafmec.2024.104415.

Zhang, B.C., Fu, J.H., Feng, Z.C., et al., 2025a. Mechanical response of coal exposed to variable-frequency multistage uniaxial cyclic loads. Nat. Resour. Res. 34 (5), 2823–2840. https://doi.org/10.1007/s11053-025-10531-9.

Zhang, C., Jia, S., Ren, Z.P., et al., 2024a. Strength evolution characteristics of coal with different pore structures and mineral inclusions based on CT scanning reconstruction. Nat. Resour. Res. 33 (6), 2725–2742. https://doi.org/10.1007/s11053-024-10397-3.

Zhang, H.B., Wang, L.H., Li, J.L., et al., 2023. Study on the mechanical properties of unloading damaged sandstone under cyclic loading and unloading. Sci. Rep. 13 (1), 7370. https://doi.org/10.1038/s41598-023-33721-y.

Zhang, L., Wang, Y.M., Gao, M.Z., et al., 2024b. Spatio-temporal evolution of pore and fracture structures in coal induced by initial damage and creep behavior: a real-time NMR-Based approach. Int. J. Min. Sci. Technol. 34 (10), 1409–1425. https://doi.org/10.1016/j.ijmst.2024.09.003.

Zhang, L.M., Ning, Z.G., Miao, S.J., et al., 2026a. Experimental and numerical investigations on the mixed-mode fracture of granite under offset three-point bending loads. Rock Mech. Rock Eng. 59 (1), 1223–1251. https://doi.org/10.1007/s00603-025-04871-4.

Zhang, L.M., Wang, M., Zhang, B., et al., 2025b. Damage mechanism of coal samples under the coupling effect of sulfate erosion and wet-dry cycles: experiments, constitutive models, and numerical simulations. Phys. Fluids 37 (7), 073398. https://doi.org/10.1063/5.0281708.

Zhang, T.C., Li, J.X., Zhu, Y.R., et al., 2025c. Impact of gas adsorption on coal relative permeability: a laboratory study. Int. J. Rock Mech. Min. Sci. 194, 106191. https://doi.org/10.1016/j.ijrmms.2025.106191.

Zhang, T.C., Zhu, Y.R., Li, J.X., et al., 2026b. Impact of effective stress on coal relative permeability: experiment and model development. Rock Mech. Rock Eng. 59 (3), 3915–3938. https://doi.org/10.1007/s00603-025-05020-7.

Zhang, X.M., Zhang, D.M., Leo, C.J., et al., 2017. Damage evolution and post-peak gas permeability of raw coal under loading and unloading conditions. Transp. Porous Medium. 117 (3), 465–480. https://doi.org/10.1007/s11242-017-0842-z.

Zhao, J.J., Tian, S.X., Wen, Y.H., et al., 2026. Boosting coalbed methane recovery through nanofluid-mediated pore and interfacial regulation. Process Saf. Environ. Prot. 207, 108247. https://doi.org/10.1016/j.psep.2025.108247.

Zhu, C., Chen, J., Pu, Y.Y., et al., 2025. Mechanism of non-blasting supercritical CO_2 fracturing in rocks under reverse fault conditions: Dynamic and quantitative monitoring using coda waves. Rock Mech. Rock Eng. 58 (2), 2367–2385. https://doi.org/10.1007/s00603-024-04203-y.

Zou, J.P., Chen, W.Z., Yang, D.S., et al., 2016. The impact of effective stress and gas slippage on coal permeability under cyclic loading. J. Nat. Gas Sci. Eng. 31, 236–248. https://doi.org/10.1016/j.jngse.2016.02.037.

Zou, Q.L., Chen, Z.H., Zhan, J.F., et al., 2023. Morphological evolution and flow conduction characteristics of fracture channels in fractured sandstone under cyclic loading and unloading. Int. J. Min. Sci. Technol. 33 (12), 1527–1540. https://doi.org/10.1016/j.ijmst.2023.11.003.

Zou, Q.L., Liu, Y., Li, Q.S., et al., 2025a. Effect of particle size and dosage on hydration kinetics of nano-alumina-modified cement. Constr. Build. Mater. 494, 143283. https://doi.org/10.1016/j.conbuildmat.2025.143283.

Zou, Q.L., Ma, T.F., Liang, J.Y., et al., 2025b. Mesomechanical weakening mechanism of coal modified by nanofluids with disparately sized SiO_2 nanoparticles. Int. J. Rock Mech. Min. Sci. 188, 106056. https://doi.org/10.1016/j.ijrmms.2025.106056.